

X-RAY PERSPECTIVE OF THE TWISTED MAGNETOSPHERES OF MAGNETARS

SHAN-SHAN WENG¹, ERSIN GÖĞÜŞ¹, TOLGA GÜVER², & LIN LIN³

¹ Sabancı University, Faculty of Engineering and Natural Sciences, Orhanlı Tuzla 34956 Istanbul Turkey

² Istanbul University, Science Faculty, Department of Astronomy and Space Sciences, Beyazıt, 34119, Istanbul, Turkey and

³ François Arago Centre, APC, Université Paris Diderot, CNRS/IN2P3 13 rue Watt, 75013 Paris, France

Draft version May 25, 2015

ABSTRACT

Anomalous X-ray pulsars (AXPs) and soft gamma-ray repeaters (SGRs) are recognized as the most promising magnetar candidates, as indicated by their energetic bursts and rapid spin-downs. It is expected that the strong magnetic field leaves distinctive imprints on the emergent radiation both by affecting the radiative processes in atmospheres of magnetars and by scattering in the upper magnetospheres. We construct a self-consistent physical model that incorporates emission from the magnetar surface and its reprocessing in the three-dimensional (3D) twisted magnetosphere using a Monte Carlo technique. The synthetic spectra are characterized by four parameters: surface temperature kT , surface magnetic field strength B , magnetospheric twist angle $\Delta\phi$, and the normalized electron velocity β . We also create a tabular model (STEMS3D) and apply it to a large sample of *XMM-Newton* spectra of magnetars. The model successfully fits nearly all spectra, and the obtained magnetic field for 7 out of the 11 sources are consistent with the values inferred from the spin-down rates. We conclude that the continuum-fitting by our model is a robust method to measure the magnetic field strength and magnetospheric configuration of AXPs and SGRs. Investigating the multiple observations of variable sources, we also study the mechanism of their spectral evolution. Our results suggest that the magnetospheres in these sources are highly twisted ($\Delta\phi > 1$), and the behavior of magnetospheric twisting and untwisting is revealed in the 2002 outburst of 1E 2259+586.

Subject headings: radiation mechanisms: nonthermal — stars: magnetic fields — stars: neutron — X-rays: stars

1. INTRODUCTION

Anomalous X-ray pulsars (AXPs) and soft gamma-ray repeaters (SGRs) form an intriguing class of isolated neutron stars (NSs). They share the similar observational properties: (1) relatively slow spin periods ($P \sim 2 - 12$ s); (2) large spin-down rates ($\dot{P} \sim 10^{-14} - 10^{-10}$ s s⁻¹); (3) high persistent X-ray luminosity ($L_X \approx 10^{34} - 10^{36}$ erg s⁻¹), which significantly exceeds their rotation power for most sources; and (4) different types of X-ray variability; i.e., long-term X-ray flux enhancements and short energetic bursts (see Mereghetti 2008, and Rea & Esposito 2011 for recent reviews). These behaviors can be understood within the magnetar scenario – extremely strong magnetic fields of some NSs giving rise to the observed exotic manifestations (Thompson & Duncan 1995, 1996). There are now 28 magnetars or magnetar candidates known¹ (Olausen & Kaspi 2014; Zhou et al. 2014).

Although recent multi-wavelength observations of magnetar activities significantly widened our views, the most essential knowledge on magnetars is provided by the emission properties of their X-ray radiation. The X-ray spectra of SGRs and AXPs below 10 keV are soft and can be empirically described by a power-law (PL) model with photon index $\Gamma \sim 2 - 4$ and a thermal component with temperature $kT \sim 0.5$ keV (Mereghetti et al. 2005, 2006). Also note that it has been revealed that some magnetars exhibit a very hard spectrum ($\Gamma \sim 1$) above 10 keV (see, e.g., Kuiper et al. 2004, 2006; den Hartog et al.

2008a,b). Beloborodov (2013) suggested that the hard X-ray emissions attribute to surface emissions scattered by the relativistic outflows around magnetars, which also make a non-negligible contribution below 10 keV. Studying the spectra of persistent emission, Marsden & White (2001) reported that the hardness of the spectra increases with the spin-down rate $\dot{\nu}$. With more accumulated data, Kaspi & Boydstun (2010) showed that the spectral indices in quiescence are not only correlated with $\dot{\nu}$ but also the magnetic field B inferred from timing analyses. Magnetars occasionally emit short (~ 0.1 s) bursts, during which the plausible line features have been also detected in some sources (e.g., Strohmayer & Ibrahim 2000). If such features are due to the proton cyclotron absorption, the inferred magnetic field somehow deviates from the value estimated from the spin-down rate (e.g., Woods et al. 2005; Tiengo et al. 2013; An et al. 2014). An independent method is thus required to evaluate the magnetic field of magnetars.

In the magnetar framework, the X-ray radiation can be physically interpreted as the NS surface emission scattered by the plasma in the magnetosphere (see, e.g., Thompson et al. 2002; Lyutikov & Gavril 2006; Fernández & Thompson 2007; Tong et al. 2010). Thompson et al. (2002) suggested that the internal magnetic field of magnetars is highly twisted and anchored in the highly conducting crust of an NS. In starquakes, the strong internal magnetic field deforms the crust, and as a result the footpoints of the external magnetic field lines are displaced, i.e., the magnetic field outside the star – magnetosphere is also twisted. Alternatively, a twisted magnetosphere can also be aroused by

¹ <http://www.physics.mcgill.ca/~simspulsar/magnetar/main.html>

continued footpoint motions (Beloborodov 2009). The twisted external magnetic field can support electric currents that are much larger than the Goldreich-Julian current (Thompson et al. 2002; Lyutikov & Gavril 2006). The charge carriers provide large optical depth to resonant cyclotron scattering (RCS) so that soft photons can be Compton up-scattered and form a PL high-energy tail. Both one-dimensional (1D) and three-dimensional (3D) RCS models had been developed (see e.g., Lyutikov & Gavril 2006; Fernández & Thompson 2007), and offered promising fits for the X-ray spectra of SGRs/AXPs (Rea et al. 2008; Zane et al. 2009). Because the non-resonant scattering contributes a negligible fraction, both 1D and 3D RCS models only take the resonant scattering into consideration. For \sim keV photons, the resonant scattering occurs in the layer where the magnetic field decays to $\sim 10^{11}$ G regardless of the NS surface magnetic field. As a consequence, the essential information of SGRs/AXPs – the strength of the magnetic field—is not incorporated in both 1D and 3D RCS models since the scattering process is insensitive to the magnetic field below its cyclotron frequency (≥ 100 keV for a magnetar magnetic field).

Besides the magnetospheric scattering, the surface emissions are also distorted in strongly magnetized ($B \geq 10^{13}$ G) NS atmospheres due to the effect of vacuum polarization and proton cyclotron resonances, by affecting the interactions between the photons and the plasma (e.g., Ho & Lai 2003; Özel 2003). Thus, the spectral profile of surface emission strongly depends on the magnetic field. Taking into account the combined effects of the magnetar atmosphere and its magnetosphere, Güver et al. (2007) developed the 1D surface thermal emission and magnetospheric scattering (STEMS) model, which can successfully fit the soft X-ray spectra of both steady and variable magnetars (Güver et al. 2007, 2012; Ng et al. 2011; Lin et al. 2012). Additionally, the STEMS model uncovers the information concerning the magnetic field. However, because the STEMS model treats the scattering region as a plane-parallel slab, it cannot offer information about the geometry of the magnetosphere.

The long-term monitoring observations revealed that the X-ray emissions of most magnetars are variable (e.g., Rea 2014), in the extreme cases, namely the transient magnetars (e.g., XTE J1810-197, and 1E 1547.0-5408), the overall flux can be enhanced up to three orders of magnitude brighter than their quiescent level (e.g., Ibrahim et al. 2004; Mereghetti et al. 2009; Kaneko et al. 2010). Studying X-ray behaviors in different flux levels would help us to explore the nature of magnetar, i.e., the evolution of magnetospheres (Beloborodov 2009) and the magneto-thermal evolution of NSs (Pons & Rea 2012; Viganò et al. 2013). Based on *XMM-Newton* observations, Zhu et al. (2008) found that the afterglow of the 1E 2259+586’s 2002 outburst followed by a PL decay and the hardness is strongly correlated with the flux. Alternatively, the flux relaxation of XTE J1810-197’s 2003 outburst is best described by an exponential decay and the surface temperature became cold in the meantime (Gotthelf & Halpern 2005). Diverse observational phenomena (see Rea & Esposito 2011 and reference therein) suggest that X-ray activi-

ties could be driven by different mechanisms, either the twisted magnetospheres (Thompson et al. 2002) or the deep crustal heating (Lyubarsky et al. 2002).

In this work, we carry out 3D Monte Carlo simulations of the emitted photons from the surface of a highly magnetized NS propagation in a twisted magnetosphere. The physical bases of our model and the Monte Carlo method are described in Section 2. The model properties are presented in Section 3. We also numerically calculate model spectra and create a tabular model, which is further applied to the X-ray spectra of magnetars (Section 4). The ultimate goal of this paper is to better understand the surface and magnetospheric properties of magnetars and their evolutions using our model. In Section 5, we discuss the spectral modeling results and their implications.

2. MODELS

In this section, we first outline the physical processes in a strongly magnetized atmosphere, and then scatter the surface emission in the 3D twisted magnetosphere. The gravitational redshift effect is also considered in our model.

2.1. Surface emission of magnetars

In strong magnetic fields ($B \geq 10^{13}$ G), the vacuum polarization, a quantum electrodynamics phenomenon, can affect radiative transfer in magnetized plasmas by modifying polarization modes and the opacities of the normal modes (e.g., Zane et al. 2001; Ho & Lai 2003; Özel 2003). The proton cyclotron resonance is another phenomenon that affects the propagation of photons in a magnetized plasma. Following the methods discussed in Özel (2001, 2003), the radiative equilibrium models are constructed for the fully ionized hydrogen plasmas, taking into account the effects of vacuum polarization and ion cyclotron lines. We use a modified Feautrier method for the solution of the angle- and polarization-mode dependent radiative transfer problem and ensure radiative equilibrium with a temperature correction scheme based on the Lucy–Unsöld algorithm. The surface emission spectrum can be defined by just two parameters: the effective temperature of atmosphere kT and the surface magnetic field strength B .

2.2. Resonant cyclotron scattering in 3D twisted magnetosphere

The Monte Carlo techniques are quite suitable to handle photon scattering in complicated 3D configurations and the 3D RCS Monte Carlo code has already been built by Fernández & Thompson (2007) and Nobili et al. (2008). Both of these works considered axisymmetric globally twisted magnetospheres and seed photons as being the canonical blackbody (BB) emissions. Nevertheless, these codes allow for an arbitrary distribution of seed photons, velocity distribution of the charged particles, and magnetic field geometry.

We build our Monte Carlo code following an approach that is similar to the one discussed in Nobili et al. (2008). The fundamental difference is the description of seed photons. (1) The original BB emissions are distorted after travelling through strongly magnetized atmospheres, mostly carried by extraordinary mode photons (Özel 2003). In our work, this surface emission is adopted as

the seed photons, which are homogeneously injected from the stellar surface with a wavevector pointing in the radial direction. Note that under the influence of an ultra-strong magnetic field, the surface emissions are expected to be anisotropic and their temperature varies with latitude (e.g., Heyl & Hernquist 1998; Bernardini et al. 2011). However, the study on the anisotropic surface emissions is beyond the scope of this paper and will be reported elsewhere. (2) The globally twisted magnetosphere has a self-similar and force-free construction ($\mathbf{j} \times \mathbf{B} = 0$), which is uniquely characterized by the net twist angle of the field lines anchored close to the two magnetic poles, $\Delta\phi$. (3) The current density \mathbf{j} is deduced from the Ampere's law ($\nabla \times \mathbf{B} = (4\pi/c)\mathbf{j}$) under the force-free assumption. Following the work in Nobili et al. (2008), we consider the effects of bulk velocity and also thermal velocity distribution of charge carriers, assuming a 1D Maxwellian distribution at a given temperature superimposed to a bulk motion. In order to reduce parameters in the model, the electron temperature kT_e is derived from the bulk velocity (and further halved) by assuming the equipartition between thermal and bulk kinetic energy. As a result, the number density of electrons (n_e) is a function of the twist angle and the average electron velocity. (4) We neglect both the non-resonant scattering and electron recoil effects, which are not important in the soft X-ray band. The spectrum is calculated in the non-relativistic regime with the simplified resonant cross-section (Equation (10) in Nobili et al. 2008), which is independent of magnetic field and frequency.

As photons propagate in the 3D twisted magnetosphere, we check whether they can freely escape out of the magnetosphere in every step (Fernández & Thompson 2007; Nobili et al. 2008). If the photon frequency together with moving direction still allow resonant scattering, as soon as the integrated scattering depth τ_s satisfies $\tau_s \geq -\ln U$, where U is a random number in the range $[0,1]$, a scattering is triggered, and the photon frequency, direction, and polarization are updated. Then, the photon continues to travel in the magnetosphere until another scattering occurs or it escapes to infinity (observers). We also refer to Nobili et al. (2008) for more details on the scattering process. The spectra are calculated by evolving 5,000,000 photons and characterized by four parameters: surface temperatures kT , magnetic field strength at the poles B , magnetospheric twist angles $\Delta\phi$, and the normalized electron velocity $\beta = v/c$, where c is the speed of light. An example spectrum ($kT = 0.3$ keV, $B = 10^{14}$ G, $\Delta\phi = 1.0$, and $\beta = 0.3$) is shown in Figure 1.

2.3. Gravitational redshift effect

Because of the strong gravitational field of NSs, the gravitational redshift effect is important and should be corrected for the photons close to NSs, but is negligible for the photons that are far away from NSs ($>$ several times of the NSs radii). According to General Relativity, the photons experience a redshift in gravitational fields by a factor of $1 + z = \frac{1}{\sqrt{1 - \frac{2GM}{Rc^2}}}$ assuming Schwarzschild geometry. In principle, the gravitational redshift should be corrected for the surface emission, before the magnetospheric scattering. Since the scattering optical depth

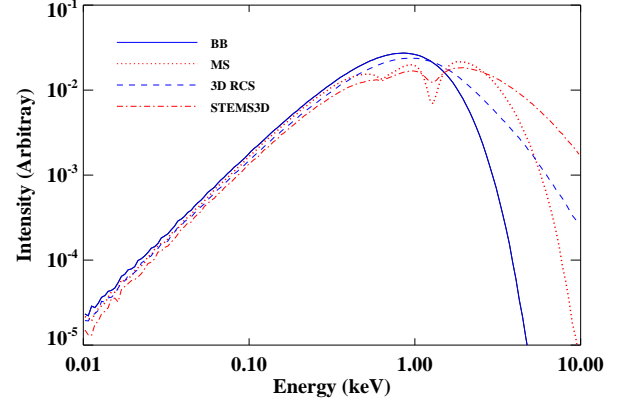


Figure 1. The BB ($kT = 0.3$ keV, blue solid line) and the magnetar surface (MS, $kT = 0.3$ keV and $B = 10^{14}$ G, red dotted line) emissions are scattered in a 3D twisted magnetosphere ($\Delta\phi = 1.0$ and $\beta = 0.3$), resulting in the spectra of the 3D RCS (blue dashed line) and the STEMS3D (red dotted-dashed line), respectively.

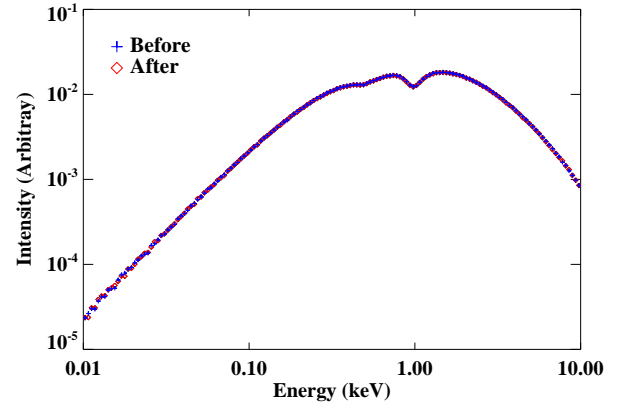


Figure 2. Example spectrum ($kT = 0.3$ keV, $B = 10^{14}$ G, $\Delta\phi = 1.0$, and $\beta = 0.3$) with the gravitational redshift correction ($z = 0.306$) performed before (blue plus) and after (red diamond) the magnetospheric scattering.

is independent of frequency in a self-similar magnetosphere (Thompson et al. 2002; Fernández & Thompson 2007), it allows us to correct the spectra after the magnetospheric scattering. In order to test this hypothesis, we calculated the spectra for $kT = 0.3$ keV, $B = 10^{14}$ G, $\Delta\phi = 1.0$, and $\beta = 0.3$ with the gravitational redshift correction of $z = 0.306$ (corresponding to an NS with mass $1.4 M_\odot$ and $R_{\text{NS}} = 10$ km) performed before (red line in Figure 2) and after (blue line) the magnetospheric scattering, and find that both spectra are identical. Therefore, it becomes feasible and convenient to do the correction in *XSPEC* (after scattering, §4).

3. MODEL PROPERTIES

The emerging radiation from the surface of a highly magnetized NS is expected to be modified by both vacuum polarization and proton cyclotron resonance. At magnetar-type field strengths, the resulting spectrum is spectrally harder than a Planckian and would exhibit proton line features in the soft-X-ray band (Figure 1).

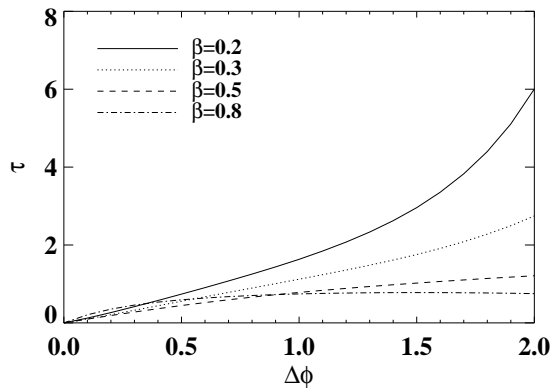


Figure 3. Angle-averaged optical depth (τ) vs. $\Delta\phi$ and different values of β : 0.2 (solid), 0.3 (dotted), 0.5 (dashed), and 0.8 (dash-dotted).

The emerging photons further gain energy by multiple scattering in the twisted magnetosphere, manifesting themselves as the high energy tail. To illustrate this point, we performed the scattering of a BB ($kT = 0.3$ keV) as well as the magnetar surface emission ($kT = 0.3$ keV and $B = 10^{14}$ G) in a 3D twisted magnetosphere ($\Delta\phi = 1.0$ and $\beta = 0.3$). We present these spectra in Figure 1. We also calculated the spectrum of the 3D RCS in the same way as the spectrum of STEMS3D model, but with a single temperature BB adopted for the seed photons.

Unlike the STEMS model, in which the optical depth is independent of the particle velocity (Lyutikov & Gavril 2006; Güver et al. 2007), the optical depth in the STEMS3D is determined by both the degree of magnetospheric twist and the velocity of charged particles. In Figure 3, we show that the variation of angle-averaged mean number of scattering per photon (τ) with respect to $\Delta\phi$ and β . Figure 4 illustrates the effects on the spectral shape of varying twist angle and electron velocity. It is clearly seen that the level of upscattering of emergent thermal photons increases with $\Delta\phi$ and in particular with β .

Lyutikov & Gavril (2006) pointed out that the deep line features present in the surface spectra can be smoothed out with a large scattering optical depth. However, investigating the spectra obtained with a narrow velocity distribution ($\beta = 0.5$, $\Delta\beta = 0.1$) and large twist ($\Delta\phi = 1.0$), Fernández & Thompson (2007) argued that the line strength can be reduced by a factor of ~ 2 ; however, a significant line feature remained as a result of an optical depth in the 3D twisted magnetosphere that was not very large. As already mentioned, the optical depth in 3D twisted magnetosphere depends not only on $\Delta\phi$ but increases sharply with decreasing β (Figure 3). As we show in Figure 4, we find that the STEMS3D model can indeed wash out the line features if the twist angle is large ($\Delta\phi \geq 1$) and the electron speed is slow ($\beta \leq 0.3$) enough.

4. APPLICATION TO SOFT X-RAY SPECTRA OF MAGNETARS

We generated model X-ray spectra in the 0.01–10.0 keV range using the numerical model described in §3.

We used the following parameter space for our numerical grid: the surface temperature $kT = 0.1 - 0.6$ keV (step 0.1 keV), surface magnetic field strength $B = 10^{14} - 10^{15}$ G (step 10^{14} G), magnetospheric twist angle $\Delta\phi = 0.0 - 2.0$ radian (step 0.1 radian), and the normalized electron velocity $\beta = 0.1 - 0.9$ (step 0.1). We then employed the routine *wftbmd*,² to create a tabular model (named STEMS3D.mod) which can be implemented into the standard package for X-ray spectral analysis, *XSPEC*. This tabular model is further applied to the observational data of magnetars.

4.1. Observations and data analysis

The main objective of our efforts here is to better understand the surface and magnetospheric properties of magnetars using the STEMS3D model. For this investigation, we selected the sources that were bright enough ($f_{0.5-10\text{keV}} \geq 10^{-12}$ erg cm $^{-2}$ s $^{-1}$) to allow statistically significant spectral results and were located in relatively low interstellar absorption ($nH \leq 5 \times 10^{22}$ cm $^{-2}$) regions of our Galaxy. When $nH > 5 \times 10^{22}$ cm $^{-2}$, X-ray emissions below 2 keV are strongly absorbed, making the parameters of the STEMS3D model unconstrained, even for the bright source SGR 1806-20. The flux of the serendipitously discovered magnetar, 3XMM J185246.6+003317, during its active phase is a few times of 10^{-12} erg cm $^{-2}$ s $^{-1}$. However, it was only detected with EPIC-MOS (Zhou et al. 2014), which has a smaller effective area. We do not include these spectra owing to the low signal-to-noise ratio (S/N).

Our sample includes bright persistent magnetars that exhibited only subtle long-term flux variations even when they experienced glitches or emitted energetic X-ray bursts 4U 0142+61 (Gavril et al. 2011); 1RXS J170849.0-400910 (Şaşmaz Muş & Göğüş 2013); 1E 1841-045 (Şaşmaz Muş et al. 2014); and SGR 1900+14 (Israel et al. 2008). On the other hand, two bright persistent sources: 1E 2259+586 and 1E 1048.1-5937 showed long-term X-ray flux enhancements in connection with X-ray bursts and glitches (Kaspi et al. 2003; Dib et al. 2009). Over the last decade, transient magnetars have emerged as a subgroup. In quiescence, these sources emit X-rays at levels near or below our detection capabilities. Their X-ray fluxes are enhanced by a factor of 100 or more at the onset of their outburst episodes (Rea 2014). We selected 1E 1547.0-5408 (Israel et al. 2008), *Swift* J1822.3-1606 (Scholz et al. 2014), SGR 0501+456 (Göğüş et al. 2010; Lin et al. 2012), and XTE J1810-197 (Güver et al. 2007) to investigate the spectral behavior of transient magnetars. Note that the quiescent spectra of transient magnetars are excluded even when their fluxes exceed the critical flux level. We discuss the implications of these spectra and limitations of our model for sources in quiescence in §5. We also include in our sample the longest *XMM-Newton* observation of CXOU J171405.7-381031 in 2010. The observational details of the X-ray data used in this paper are listed in Table 1. Note that the two short observations of 1E 1841-045 in 2002 October were performed just two days apart. To improve counting statistics, we combine these two short observations to one spectrum.

² <http://heasarc.gsfc.nasa.gov/docs/heasarc/ofwg/docs/general/model1>

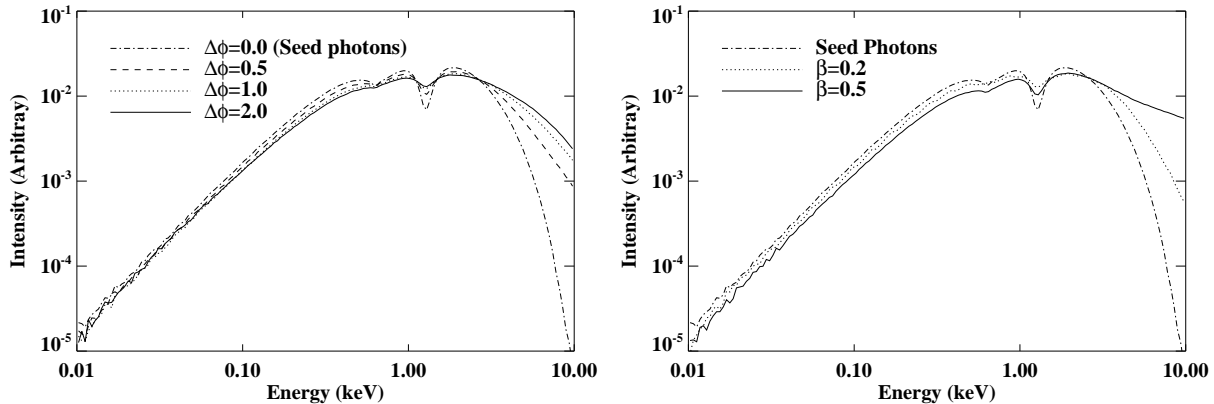


Figure 4. Left: model spectra (without gravitational redshift correction) for $B = 10^{14}$ G, $kT = 0.3$ keV, $\beta = 0.3$ and different values of $\Delta\phi$. Right: computed spectra for $B = 10^{14}$ G, $kT = 0.3$ keV, $\Delta\phi = 1.0$ and different values of β .

The data collected with the *XMM-Newton* EPIC-pn instrument are reduced using the Science Analysis System software (SAS) version 12.0.1, and filtered with the standard criteria: cleaning for background areas, setting FLAG=0 and PATTERN \leq 4. We use the SAS task *epatplot* to evaluate the pile-up fraction. For observations showing severe problems with pile-up (Table 1), spectra are extracted within annulus regions with the inner radius ~ 10 – $20''$ and ARF files are calculated to correct the missing part of the point-spread function, thus the correct flux level could still be measured through spectral fitting. The spectral response files are created using the SAS tasks *rmfgen* and *arfgn*. All spectra are rebinned with the task *specgroup* to have at least 20 counts per bin to enable the use of chi-square statistics and not to oversample the instrument energy resolution by more than a factor of three. A 2% systematic error is added to the data to account for uncertainties in instrumental calibrations. The spectral analysis is performed in the 0.5–7.0 keV energy range for the spectra having a low absorption, while in the 1.0–7.0 keV for those being highly absorbed. We note that the model-independent residuals are detected in the spectra of 1E 1547.0-5408 and CXOU J171405.7-381031 below 1.2 keV; therefore, only the spectra in the energy 1.2–7.0 keV are used (Table 1). All spectra are fitted with *XSPEC* 12.8.1 (Arnaud 1996). Because the interstellar hydrogen column density (nH) is not expected to vary during different observations, for each source with more than one pointing, we fit all available spectra simultaneously and link the nH to have a common value, and the more updated solar abundances by Lodders (2003) are adopted in our work.

We first attempt to fit all spectra with an absorbed STEMS3D model assuming the gravitational redshift parameter of 0.306. We find that spectra of 4U 0142+61 and 1RXS J170849.0-400910 clearly require an additional hard-X-ray component; therefore, adding a PL component significantly improved the fit since the mechanism responsible for the hard-X-ray emission likely contributes a non-negligible fraction of soft-X-ray emission and naturally affects our fitting (see Figure 5). We fixed the photon index Γ to the values obtained from the fitting to the contemporaneous hard-X-ray data. As the spectra from 4U 0142+61, 1RXS J170849.0-400910, 1E 1841-

045, and SGR 1900+14 above 10 keV are relatively stable and can be fitted with a PL model, we adopt a Γ of 0.93 (den Hartog et al. 2008a), 1.13 (den Hartog et al. 2008b), 1.32 (Kuiper et al. 2006), and 1.43 (Enoto et al. 2010a), respectively, in addition to STEMS3D in our spectral fitting. Because the hard-X-ray component in 1E 1547.0-5408 exhibited dramatic transient behavior (Kuiper et al. 2012), we only analyze the *XMM-Newton* observation executed on 2009 February 3, and we used a PL index Γ of 1.41 according to the Suzaku HXD-PIN data on 2009 January 28 (Enoto et al. 2010b).

4.2. Spectral analysis, spectral evolution, and correlations

4.2.1. Persistent Magnetars

4U 0142+61 is the brightest magnetar and has been one of the most stable X-ray emitters in X-rays (Gonzalez et al. 2010; Wang et al. 2014). Its longest *XMM-Newton* spectra in the 0.5–7.0 keV band can be modeled perfectly with an absorbed STEMS3D plus a PL. We find the surface temperature, $kT = 0.33$ keV, and surface magnetic field, $B = 5.87 \times 10^{14}$ G (see Table 2 for all other fit details and Figure 6 for the unfolded spectrum and best-fit model curve). Note that these surface parameters are consistent with those that were obtained using STEMS (Güver et al. 2007). We find that the magnetospheric electrons are non-relativistic ($\beta=0.21$), and that the magnetospheric twist angle, $\Delta\phi = 1.77$, that is close to upper end of our parameter space. The STEMS3D component contributes more than 98% of the total flux below 7 keV.

Since the first glitch activity detected in 1999 (Kaspi et al. 2000), several glitches were unveiled in 1RXS J170849.0-400910 (Şaşmaz Muş & Göğüş 2013). The source emits persistent radiation in both soft- and hard-X-rays. Fitting the 0.5–7.0 keV spectrum, we find that the surface temperature is relatively high ($kT = 0.49$ keV) and the other parameters are quite close to those in 4U 0142+61, i.e., $B = 6.03 \times 10^{14}$ G, $\Delta\phi = 1.82$, and $\beta = 0.20$ (Table 2). The STEMS3D component contributes about 88% of the total soft-X-ray flux (Figure 6).

The AXP 1E 1841-045 is located at the center of the X-ray and radio supernova remnant (SNR) Kes 73

Table 1
Log of the *XMM-Newton* observations used in this work

Source	Obs No.	ObsID	Obs Date	Mode	Net Exposure (ksec)	Energy band (keV)
4U 0142+61 [#]	Obs1	0206670101	2004 Mar 01	Timing	37	0.5-7.0
1RXS J170849.0-400910 [#]	Obs1	0148690101	2003 Aug 28	SW	31	0.5-7.0
1E 1841-045 [#]	Obs1	0013340101	2002 Oct 05	LW	2	1.0-7.0
...	...	0013340201	2002 Oct 07	LW	4	...
SGR 1900+14 [#]	Obs1	0305580101	2005 Sep 20	FF	21	1.0-7.0
...	Obs2	0305580201	2005 Sep 22	FF	20	...
...	Obs3	0410580101	2006 Apr 01	FF	14	...
...	Obs4	0506430101	2008 Apr 08	FF	23	...
1E 1048.1-5937	Obs1	0112780401	2000 Dec 28	FF	4	0.5-7.0
...	Obs2	0147860101 [†]	2003 Jun 16	FF	46	...
...	Obs3	0164570301	2004 Jul 08	Timing	31	...
...	Obs4	0307410201	2005 Jun 16	SW	19	...
...	Obs5	0307410301	2005 Jun 28	SW	16	...
...	Obs6	0510010601	2007 Jun 14	SW	34	...
...	Obs7	0654870101	2011 Aug 06	FF	76	...
...	Obs8	0723330101 [†]	2013 Jul 22	FF	54	...
1E 2259+586	Obs1	0057540101 [†]	2002 Jan 22	FF	10	0.5-7.0
...	Obs2	0038140101	2002 Jun 11	SW	34	...
...	Obs3	0155350301	2002 Jun 21	SW	18	...
...	Obs4	0057540201 [†]	2002 Jul 09	FF	7	...
...	Obs5	0057540301 [†]	2002 Jul 09	FF	11	...
...	Obs6	0203550301 [†]	2004 Feb 20	FF	4	...
...	Obs7	0203550601	2004 Jun 06	SW	5	...
...	Obs8	0203550401	2004 Jun 22	SW	4	...
...	Obs9	0203550501	2004 Dec 19	SW	4	...
...	Obs10	0203550701	2005 Jul 28	SW	3	...
CXOU J171405.7-381031	Obs1	0606020101	2010 Mar 17	FF	81	1.2-7.0
XTE J1810-197	Obs1	0161360301	2003 Sep 08	SW	7	0.5-7.0
...	Obs2	0161360501	2004 Mar 11	LW	10	...
...	Obs3	0164560601	2004 Sep 18	LW	23	...
...	Obs4	0301270501	2005 Mar 18	LW	36	...
SGR 0501+456	Obs1	0560191501	2008 Aug 23	SW	34	0.5-7.0
...	Obs2	0552971101	2008 Aug 29	SW	17	...
...	Obs3	0552971201	2008 Aug 31	SW	7	...
...	Obs4	0552971301	2008 Sep 02	SW	14	...
...	Obs5	0552971401 [†]	2008 Sep 30	LW	28	...
<i>Swift</i> J1822.3-1606	Obs1	0672281801 [†]	2011 Sep 23	LW	10	0.5-7.0
...	Obs2	0672282701 [†]	2011 Oct 12	LW	17	...
...	Obs3	0672282901	2012 Apr 05	LW	23	...
...	Obs4	0672283001	2012 Sep 08	LW	20	...
1E 1547.0-5408 [#]	Obs1	0560181101 [†]	2009 Feb 03	FF	49	1.2-7.0
SGR 0418+5729	Obs1	0610000601	2009 Aug 12	SW	41	0.5-7.0
CXOU J164710.2-455216	Obs1	0404340101	2006 Sep 22	FF	40	1.0-7.0
...	Obs2	0410580601	2007 Feb 17	LW	16	...
...	Obs3	0505290201	2007 Aug 19	LW	22	...
...	Obs4	0505290301	2008 Feb 15	LW	19	...
...	Obs5	0555350101	2008 Aug 20	LW	28	...
...	Obs6	0679380501	2011 Sep 27	LW	15	...

Note. — Mode: operating mode of the EPIC-pn including full-frame (FF), large-window (LW), small-window (SW), and timing modes. Net exposure: clean exposure (in unit of kiloseconds) after background flares excluded. energy band: Energy band in which spectra are fitted with *XSPEC*.

[#]: Sources' spectra are fitted by the absorbed (STEMS3D+PL) model with the PL index Γ fixed (see the text for more details), and the others are fitted by a single absorbed STEMS3D model.

[†]: Observations suffer problems with pile-up, and spectra are extracted from annular regions centered on the source position.

(Vasist & Gotthelf 1997) and has the slowest spin period of ~ 11.8 s (Dib et al. 2008). The broadband (1–200 keV) X-ray spectrum can be described by a BB plus a single PL model (Rea et al. 2008). As can be seen in Figure 6, the PL component only supplies $\sim 8\%$ of the total flux below 7 keV; however, it starts to overcome the STEMS3D component around 5 keV. The fitting results indicate that the magnetosphere is modestly twisted ($\Delta\phi = 0.31$) and the electrons have the fastest velocity ($\beta = 0.28$) among all sources studied here, i.e., the smallest optical depth in the magnetosphere (Figure 3). The model parameters, however, have relative large errors be-

cause of the short effective exposure (~ 6 ks) in addition to high interstellar absorption.

CXOU J171405.7-381031 is associated with the SNR CTB 37B and probably with a TeV source HESS J1713-381 (Aharonian et al. 2008). CXOU J171405.7-381031 was identified as the youngest magnetar with a characteristic age of ~ 950 yr (Sato et al. 2010). There have been only modest flux variations (less than a factor of two) reported with two Chandra and one *XMM-Newton* observations during 2007 February and 2010 March (Sato et al. 2010). Currently, no model provides a good fit to its X-ray spectra below ~ 1.2 keV, likely

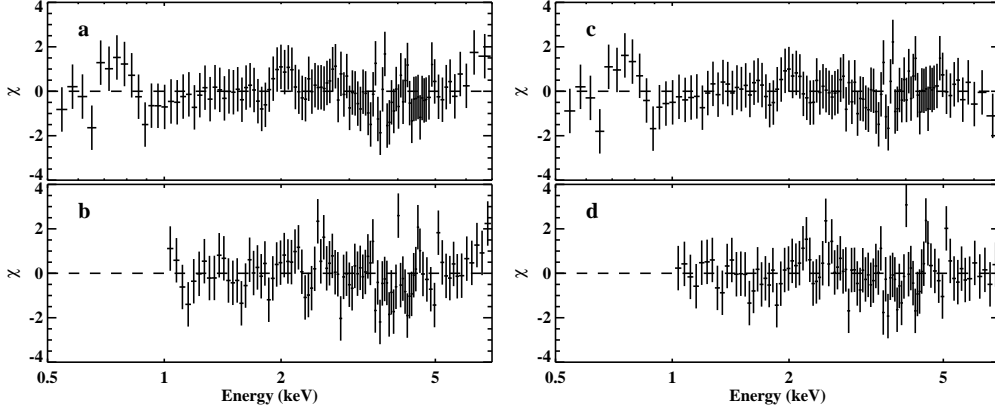


Figure 5. Spectra of 4U 0142+61 and 1RXS J170849.0-400910 are fitted with the single absorbed STEMS3D model, and the fit residuals are shown in panels (a), (b), respectively. Panels (c) and (d) plot the residuals when the same spectra are fitted with the absorbed (STEMS3D+PL) model.

Table 2
Spectral fit results of 4U 0142+61, 1RXS J170849.0-400910, and 1E 1841-045

Source	nH (10^{22} cm^{-2})	kT (keV)	B (10^{14} G)	$\Delta\phi$ (rad)	β	Flux	χ^2/dof
4U 0142+61	$0.73^{+0.03}_{-0.05}$	$0.33^{+0.03}_{-0.03}$	$5.87^{+0.68}_{-0.49}$	$1.77^{+0.09}_{-0.06}$	$0.21^{+0.01}_{-0.01}$	11.7	80.2/122
1RXS J170849.0-400910	$1.50^{+0.05}_{-0.04}$	$0.49^{+0.01}_{-0.02}$	$6.03^{+0.30}_{-0.14}$	$1.82^{+0.08}_{-0.08}$	$0.20^{+0.01}_{-0.01}$	3.26	85.2/109
1E 1841-045	$4.79^{+0.81}_{-1.19}$	$0.24^{+0.20}_{-0.07}$	$4.16^{+0.81}_{-0.36}$	$0.31^{+0.80}_{-0.11}$	$0.28^{+0.04}_{-0.06}$	1.61	178.4/161

Note. — Flux: 0.5–7.0 keV absorbed flux in units of $10^{-11} \text{ erg cm}^{-2} \text{ s}^{-1}$. All errors are in the 90% confidence level.

due to the contamination of diffuse nonthermal X-rays around the source (in the SNR). We, therefore, investigate its 1.2–7.0 keV spectrum with a single STEMS3D model, and obtain $nH = 4.39^{+0.33}_{-0.23} \times 10^{22} \text{ cm}^{-2}$, $kT = 0.51^{+0.04}_{-0.02} \text{ keV}$, $B = 9.73^{+0.59}_{-0.59} \times 10^{14} \text{ G}$, $\Delta\phi = 0.80^{+0.14}_{-0.37}$, $\beta = 0.25^{+0.05}_{-0.03}$, absorbed flux in 0.5–7.0 keV of $1.5 \times 10^{-12} \text{ erg cm}^{-2} \text{ s}^{-1}$, and $\chi^2/\text{dof} = 121.4/98$. Owing to the lowest flux and a large value of nH , we cannot obtain the upper error of B , which turns out to be the strongest surface magnetic field estimate among all sources.

SGR 1900+14 is another source whose broadband spectra (1–200 keV) can be modeled with a BB plus a single PL component. Vrba et al. (2000) reported that this source is embedded in a cluster of high-mass stars, at $\sim 12 - 15 \text{ kpc}$ away. We fit the four *XMM-Newton* spectra of SGR 1900+14 in the 1.0–7.0 keV range in order to eliminate large deviations at the low energy most likely due to the absorption by the dense gas/dust in the cluster. We find that the surface temperature remains constant within errors among these observations (see Table 3). It is also not likely that the surface magnetic field strength varies over the course of about 2.5 yr of observational span. We, therefore, link kT and B in our simultaneous fit so that our modeling would yield a common value for these two surface parameters. We find that $B = 8.0 \times 10^{14} \text{ G}$, $kT = 0.54 \text{ keV}$, $\beta \sim 0.11$, and the twist angle is less constrained. If we further tie β and $\Delta\phi$ but allow the PL and STEMS3D normalizations to vary, we obtain the equivalently good fits ($\chi^2/\text{dof} = 361.9/392$), with best-fit parameters of $B = 7.81 \times 10^{14} \text{ G}$, $kT = 0.56 \text{ keV}$, $\Delta\phi = 1.92$, and the β hit the lower limit (0.1) of pa-

rameter space (Table 3). These results suggest that the physical parameters do not evolve and SGR 1900+14 is a stable emitter. The ratio between the PL flux and the STEMS3D flux in 0.5–7.0 keV is $\sim 30/70$ (Figure 8).

4.2.2. Variable Magnetars

1E 1048.1-5937 and 1E 2259+586 are two bright magnetar sources, whose persistent X-ray flux varied by a factor of 10 or more over the timescale of months (Dib et al. 2009; Zhu et al. 2008). Dib et al. (2009) performed a comprehensive timing analysis on $\sim 10 \text{ yr}$ RXTE data of 1E 1048.1-5937, and showed that all three pulsed flares were accompanied by temporal events, e.g., significant pulse profile changes and/or a glitch. The infrared enhancement was also reported at the onset of the 2001 flare (Wang & Chakrabarty 2002). We fit all spectra of 1E 1048.1-5937 with the single STEMS3D model (Figure 9) and find that the strength of the surface magnetic field remains $\sim 2.4 \times 10^{14} \text{ G}$ (see Group 1 in Table 4). By linking the B parameter for all observations, we find that the kT varies in the range of 0.39–0.54 keV, $B = 2.42 \times 10^{14} \text{ G}$, $\Delta\phi > 1.0$, and β in the range of 0.12–0.16. In order to provide constraints on the magnetospheric parameters, in addition to B , we link the kT , $\Delta\phi$, and β for Obs1 and Obs8, kT and β for Obs5 and Obs7, and kT only for Obs3 and Obs4. This grouping improves the fit quality slightly ($\chi^2/\text{dof} = 1113.9/915$, Group 3 in Table 4). Based on these results, we investigated any possible correlations among the parameters of kT , β , and 0.5–7.0 keV flux. We find that kT is correlated with flux (the Spearman’s rank correlation coefficient, $\rho = 0.788$, the probability of obtaining such a

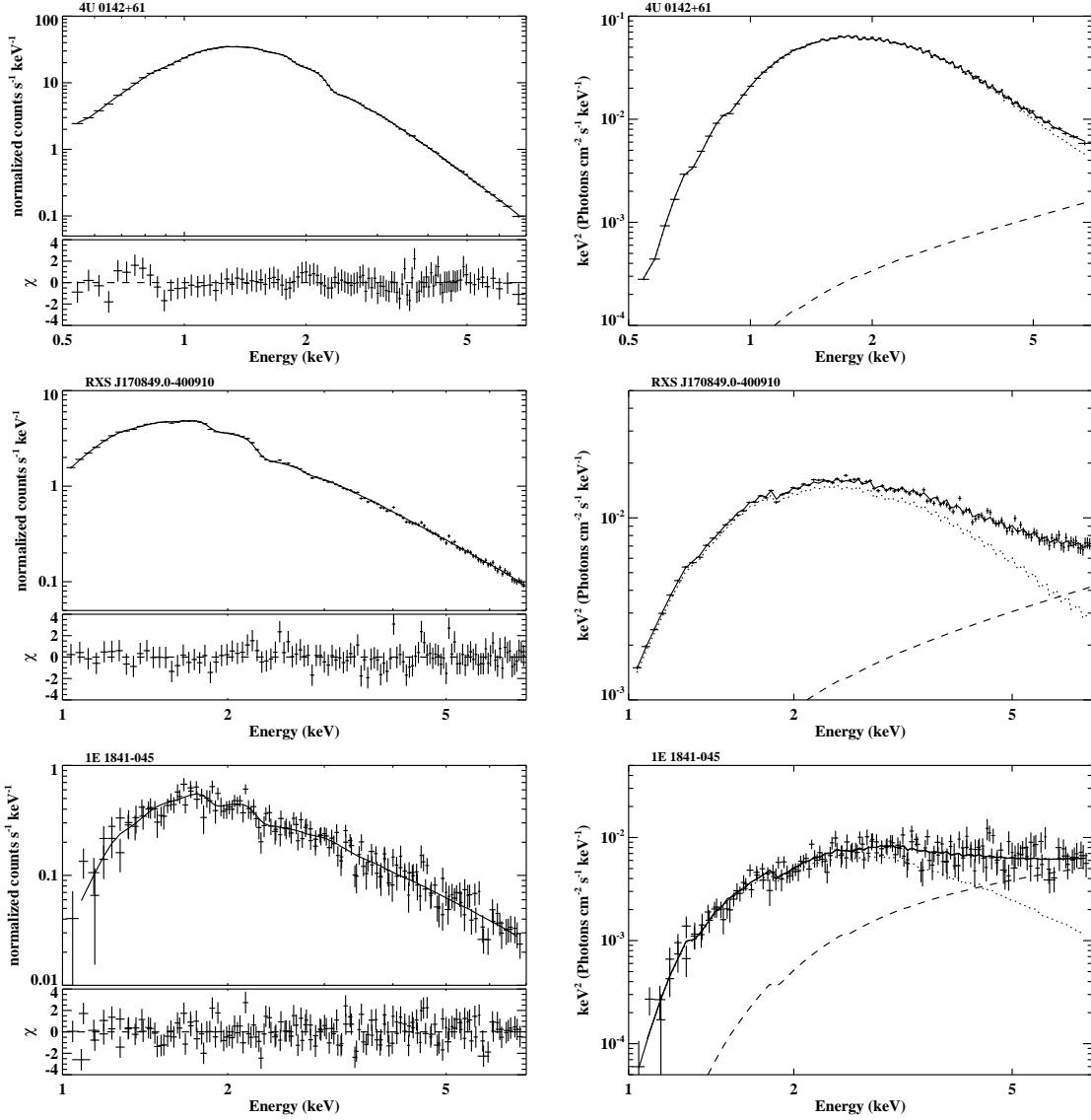


Figure 6. Left panels: the X-ray count spectra of 4U 0142+61, 1RXS J170849.0-400910, and 1E 1841-045 are fitted by the STEMS3D model (Table 2) and the residuals are shown below. Right panels: the corresponding unfolded spectra. The dotted, dashed, and solid lines in the right panels mark the STEMS3D, PL components, and the sum, respectively.

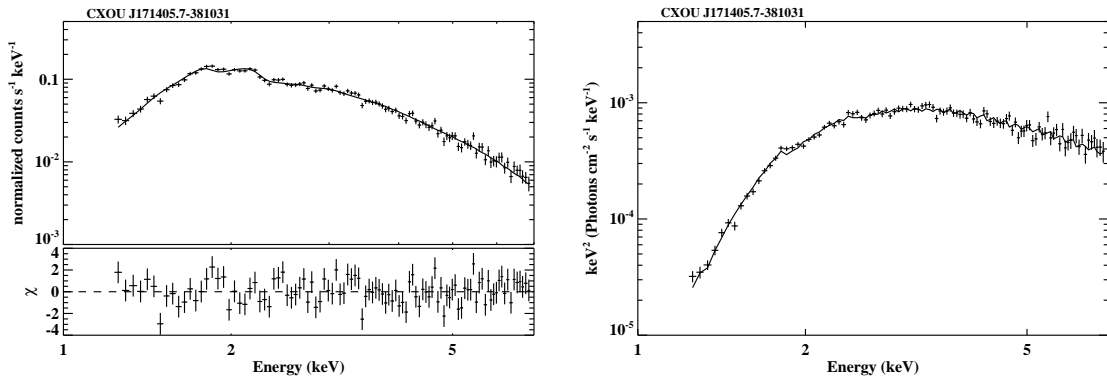


Figure 7. Same as Figure 6 but for CXOU J171405.7-381031.

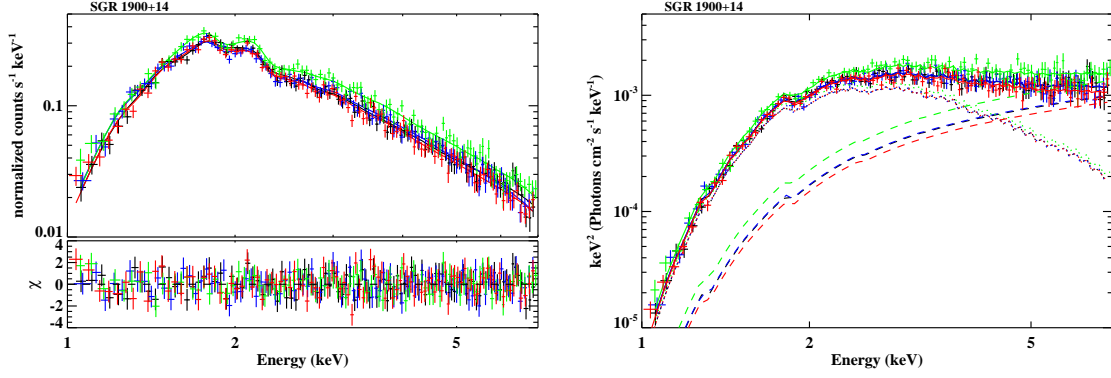


Figure 8. Left panel: spectra of SGR 1900+14 are fitted with the STEMS3D model. Different colors correspond to the four different epochs of observations and their fitting residuals are shown in the bottom panel (Table 3). Right panel: the corresponding unfolded spectra.

Table 3
Spectral parameters of SGR 1900+14

Group	Obs No.	nH (10^{22} cm^{-2})	kT (keV)	B (10^{14} G)	$\Delta\phi$ (rad)	β	Flux	χ^2/dof
Group1	Obs1	$3.60^{+0.16}_{-0.10}$	$0.48^{+0.06}_{-0.04}$	$10.0^{+0.6}_{-0.6}$	$0.81^{+0.12}_{-0.08}$	$0.15^{+0.03}_{-0.04}$	3.07	340.7/380
...	Obs2	...	$0.43^{+0.04}_{-0.18}$	$4.79^{+2.58}_{-0.64}$	$1.90^{+0.05}_{-0.89}$	$0.20^{+0.03}_{-0.03}$	3.08	...
...	Obs3	...	$0.50^{+0.08}_{-0.14}$	$8.95^{+0.53}_{-0.65}$	$1.09^{+0.87}_{-0.53}$	$0.16^{+0.06}_{-0.04}$	3.69	...
...	Obs4	...	$0.45^{+0.11}_{-0.11}$	$8.99^{+2.30}_{-2.30}$	$2.0^{+1.4}_{-1.4}$	$0.14^{+0.04}_{-0.04}$	2.93	...
Group2	Obs1	$3.45^{+0.12}_{-0.11}$	$0.54^{+0.02}_{-0.03}$	$8.00^{+0.28}_{-0.28}$	$1.86^{+0.11}_{-0.10}$	$0.10^{+0.02}_{-0.02}$	3.07	350.3/386
...	Obs2	$1.58^{+0.06}_{-0.05}$	$0.11^{+0.02}_{-0.02}$	3.09	...
...	Obs3	$2.0^{+0.1}_{-0.1}$	$0.12^{+0.02}_{-0.02}$	3.68	...
...	Obs4	$1.87^{+0.08}_{-0.06}$	$0.10^{+0.02}_{-0.02}$	2.93	...
Group3	Obs1	$3.46^{+0.13}_{-0.12}$	$0.56^{+0.01}_{-0.04}$	$7.81^{+0.61}_{-0.21}$	$1.92^{+0.07}_{-0.06}$	$0.10^{+0.04}_{-0.04}$	3.07	361.9/392
...	Obs2	3.09	...
...	Obs3	3.68	...
...	Obs4	2.93	...

Note. — Flux: 0.5–7.0 keV absorbed flux in units of $10^{-11} \text{ erg cm}^{-2} \text{ s}^{-1}$. All errors are in the 90% confidence level. Group1: the only parameter of nH is linked for different observations in the simultaneous fit. Group2: parameters of nH , kT , and B are linked. Group3: parameters of nH , kT , B , $\Delta\phi$, and β are linked.

correlation from a random data set, $P = 0.020$, and β is anti-correlated with kT ($\rho/P = -0.672/0.068$), as well as the flux ($\rho/P = -0.783/0.021$). It is important to note that all of these correlative behaviors emerge in all three steps of the fitting scheme presented in Table 4.

The SGR-like bursts and a coincident timing glitch event occurred in the AXP 1E 2259+586 on 2002 June 18 (Kaspi et al. 2003). The bursts and the glitch (that took place after Obs2 and before Obs3) were accompanied by the changes in the pulsed flux/profile and persistent flux/spectrum, providing the strongest evidence of plastic deformation of the crust (Woods et al. 2004). Hard-X-ray emission has been detected in 1E 2259+586 by INTEGRAL and Nustar (Kuiper et al. 2006; Vogel et al. 2014). Since the hard-X-ray tails contribute negligible flux below 7 keV, in which we are interested, their soft X-ray spectra are fitted with the single STEMS3D component (Tables 5 and Figure 9). It had been suggested by Zhu et al. (2008) that the unabsorbed *XMM-Newton* flux decay is best described by the PL and is correlated with the hardness. A simultaneous fit to all 10 observations yields a rather constant surface magnetic field strength. By linking B and refitting, we obtain $B \sim 6.17 \times 10^{14}$ G (Group 2 in Table 5). To better constrain the magnetospheric parameters, we also merged some successive observations (namely, Obs1/Obs2, Obs4/Obs5, Obs7/Obs8, and Obs9/Obs10), which have similar surface emission properties (kT) and are either before or after the bursting episode. We find that the magnetospheric twist angle rises to its maximum level following the bursting episode, and declines gradually over a timescale of two to three years. The particle velocity, on the other hand remains nearly constant around 0.2. Based on the results of Group 3 in Table 5, we find a strong correlation between $\Delta\phi$ and flux with the Spearman's rank correlation coefficient of $\rho/P = 0.942/0.005$. This is an important indication of the twisted/untwisted magnetosphere scenario, which we will elaborate on in the Discussion section.

4.2.3. Transient Magnetars

XTE J1810-197 was discovered in 2003 when it suddenly brightened by about two orders of magnitude above its quiescent flux (Ibrahim et al. 2004; Halpern & Gotthelf 2005). As it is the first transient magnetar, this source has been visited with *XMM-Newton* more than 24 times and its spectra are well studied, including investigations with STEMS (Güver et al. 2007). Due to the fact that the source shows no clear nonthermal component in quiescence, we only considered the observations during the outburst decay before 2005 March 18. There are two observations performed on 2003 September 8, and their spectral fitting results are consistent with each other. However, the S/N ratio of the second one (ObsID = 0161360401) is relatively low (due to its short exposure time of < 1 ks) and is excluded here. The surface temperature declines monotonically (from 0.52 ± 0.01 to 0.34 ± 0.01 keV) following the outburst of XTE J1810-197, while the magnetic field remains around $(2.2 - 2.6) \times 10^{14}$ G, which is consistent with those found using STEMS modeling (Güver et al. 2007). In the meantime, the $\Delta\phi$ parameter typically remains around ~ 1.7 and β reaches a lower limit of 0.1 (Table 6). We also fit all four spectra with common val-

ues of B and $\Delta\phi$, which yields $B = 2.52 \times 10^{14}$ G and $\Delta\phi = 1.66$.

SGR 0501+456 was discovered because it exhibited a series of short energetic bursts detected with multiple X-ray missions in 2008 August (Gögüş et al. 2010; Kumar et al. 2010). The first *XMM-Newton* observation of this source took place while SGR 0501+456 was still burst active; therefore, there were a few hundreds of short bursts in about 45 ks of effective exposure. In order to exclude the times of these burst events, we constructed the source light curve in a 0.1 s bin size, and then used a count rate cut-off criterion (< 55 cts s^{-1}) (Lin et al. 2012). SGR 0501+456 has also been detected in hard-X-ray band (Enoto et al. 2010a), but the hard-X-ray tail does not affect our fitting below 7 keV significantly. The soft-X-ray spectra are, therefore, fit with the STEMS3D model alone. We find that the surface magnetic field strength remains constant within errors (see Group 1 in Table 7). We refit all five spectra simultaneously to have a common value of B , and obtained it as $B = 2.35 \times 10^{14}$ G. In this case, we obtain that the speed of magnetospheric electrons declined from 0.2 to 0.15, while the twist angle showed a marginal evidence of variation between 1.5 and 1.7 (Group 2 in Table 7). Among all of the evolving parameters, we find a significant correlation between only β and the flux, with $\rho/P = 1/0$.

Swift J1822.3-1606 underwent an outburst in 2011 July (Livingstone et al. 2011). The timing analysis revealed a spin period of $P = 8.4$ s and a period derivative of $\dot{P} = 8.3 \times 10^{-14}$ s s^{-1} , which made this source the second magnetar with a low dipole magnetic field, $B_{\text{timing}} \simeq 2.7 \times 10^{13}$ G (Rea et al. 2012). Its spectral behavior during the flux decay resembles those observed from XTE J1810-197 in the 2003 outburst, whose dipole magnetic field inferred from spin parameters is $B_{\text{timing}} = 2.52 \times 10^{14}$ G (Camilo et al. 2007). The spectral evolution could be interpreted as the thermal relaxation in the NS crust (Scholz et al. 2014). The long-term monitoring data suggest that the temperature of the thermal component decreases slowly. Alternatively, the decreasing normalization, which is not presented in Table 8, indicates that the emitting region shrinks during the outburst decay (Rea et al. 2012; Scholz et al. 2014). In our investigation of this source with the STEMS3D model, we found that the surface temperature declined slightly from 0.54 ± 0.02 to 0.44 ± 0.02 keV in the first year of the outburst, and the surface magnetic field ($B \sim 2.32 \times 10^{14}$ G) and the electron velocity ($\beta \sim 0.12$) remained constant (Group 1 in Table 8). Refitting all four spectra with a linked surface magnetic field and β for all yields a significant fluctuation of $\Delta\phi$ (see Group 2 in Table 8). We also fit all spectra with the same value of $\Delta\phi$ and the chi-square increases to 433.5/429, indicating the a significant variation of $\Delta\phi$ with an F-test value lower than 0.005.

1E 1547.0-5408 was discovered in 1980 (Lamb & Markert 1981), but has shown repeated X-ray flux enhancements in recent years: its flux went up by a factor of > 50 with the 2008 October outburst and further increased to levels of ~ 3 orders brighter than its lowest flux at the onset of its 2009 January outburst (Dib et al. 2008; Kuiper et al. 2012). A transient hard-X-ray emission was also recorded with Suzaku

Table 4
Spectral parameters of 1E 1048.1-5937.

Group	Obs No.	nH (10^{22} cm $^{-2}$)	kT (keV)	B (10^{14} G)	$\Delta\phi$ (rad)	β	Flux	χ^2/dof
Group1	Obs1	$1.12^{+0.02}_{-0.01}$	$0.45^{+0.03}_{-0.03}$	$2.44^{+0.16}_{-0.21}$	$1.90_{-1.21}$	$0.14^{+0.04}_{-0.02}$	0.56	1060.6/902
...	Obs2	...	$0.46^{+0.02}_{-0.02}$	$2.38^{+0.08}_{-0.08}$	$1.96_{-0.05}$	$0.12^{+0.01}_{-0.01}$	1.39	...
...	Obs3	...	$0.42^{+0.01}_{-0.01}$	$2.45^{+0.07}_{-0.07}$	$1.46^{+0.31}_{-0.09}$	$0.13^{+0.02}_{-0.02}$	0.96	...
...	Obs4	...	$0.42^{+0.01}_{-0.01}$	$2.45^{+0.08}_{-0.09}$	$1.89^{+0.08}_{-0.06}$	$0.16^{+0.01}_{-0.01}$	0.80	...
...	Obs5	...	$0.40^{+0.01}_{-0.01}$	$2.66^{+0.11}_{-0.11}$	$2.0_{-0.1}$	$0.18^{+0.02}_{-0.02}$	0.72	...
...	Obs6	...	$0.53^{+0.01}_{-0.01}$	$2.36^{+0.05}_{-0.04}$	$1.84^{+0.02}_{-0.02}$	$0.12^{+0.01}_{-0.01}$	2.92	...
...	Obs7	...	$0.40^{+0.01}_{-0.01}$	$2.52^{+0.07}_{-0.05}$	$1.69^{+0.05}_{-0.05}$	$0.16^{+0.01}_{-0.01}$	0.54	...
...	Obs8	...	$0.43^{+0.02}_{-0.02}$	$2.30^{+0.08}_{-0.09}$	$1.03^{+0.06}_{-0.07}$	$0.16^{+0.02}_{-0.02}$	1.01	...
Group2	Obs1	$1.13^{+0.01}_{-0.01}$	$0.44^{+0.02}_{-0.02}$	$2.42^{+0.01}_{-0.03}$	$1.10_{-0.36}$	$0.16^{+0.05}_{-0.02}$	0.56	1108.3/909
...	Obs2	...	$0.47^{+0.01}_{-0.01}$...	$1.96_{-0.05}$	$0.12^{+0.01}_{-0.01}$	1.39	...
...	Obs3	...	$0.42^{+0.01}_{-0.01}$...	$1.45^{+0.09}_{-0.10}$	$0.14^{+0.01}_{-0.01}$	0.96	...
...	Obs4	...	$0.42^{+0.01}_{-0.01}$...	$1.90^{+0.07}_{-0.07}$	$0.16^{+0.01}_{-0.01}$	0.80	...
...	Obs5	...	$0.39^{+0.01}_{-0.01}$...	$2.0_{-0.1}$	$0.16^{+0.02}_{-0.02}$	0.72	...
...	Obs6	...	$0.54^{+0.01}_{-0.01}$...	$1.84^{+0.02}_{-0.02}$	$0.12^{+0.01}_{-0.01}$	2.91	...
...	Obs7	...	$0.39^{+0.01}_{-0.01}$...	$1.54^{+0.07}_{-0.08}$	$0.16^{+0.01}_{-0.01}$	0.54	...
...	Obs8	...	$0.44^{+0.01}_{-0.01}$...	$1.01^{+0.07}_{-0.06}$	$0.16^{+0.02}_{-0.02}$	1.01	...
Group3	Obs1	$1.13^{+0.02}_{-0.02}$	$0.44^{+0.01}_{-0.01}$	$2.42^{+0.03}_{-0.03}$	$1.06^{+0.10}_{-0.10}$	$0.16^{+0.02}_{-0.01}$	0.56	1113.9/915
...	Obs2	...	$0.47^{+0.01}_{-0.01}$...	$1.96_{-0.06}$	$0.12^{+0.01}_{-0.01}$	1.39	...
...	Obs3	...	$0.42^{+0.01}_{-0.01}$...	$1.45^{+0.15}_{-0.04}$	$0.13^{+0.01}_{-0.01}$	0.96	...
...	Obs4	...	= <i>obs3</i>	...	$1.90^{+0.08}_{-0.64}$	$0.16^{+0.01}_{-0.01}$	0.80	...
...	Obs5	...	$0.39^{+0.01}_{-0.01}$...	$2.0_{-0.1}$	$0.16^{+0.01}_{-0.01}$	0.72	...
...	Obs6	...	$0.54^{+0.01}_{-0.01}$...	$1.84^{+0.02}_{-0.02}$	$0.12^{+0.01}_{-0.01}$	2.91	...
...	Obs7	...	= <i>obs5</i>	...	$1.45^{+0.04}_{-0.12}$	= <i>obs5</i>	0.54	...
...	Obs8	...	= <i>obs1</i>	...	= <i>obs1</i>	= <i>obs1</i>	1.01	...

Note. — Flux: 0.5–7.0 keV absorbed flux in units of 10^{-11} erg cm $^{-2}$ s $^{-1}$. All errors are in the 90% confidence level. Group1: the only parameter of nH is linked for different observations in the simultaneous fit. Group2: both parameters of nH, and B and β are linked. Group3: β for Obs1 and Obs8, kT and β for Obs5 and Obs7, and kT only for Obs3 and Obs4 are further linked.

(Enoto et al. 2010b) and INTEGRAL (Kuiper et al. 2012) during the decay of the 2009 outburst. The broadband X-ray spectrum can be described with a BB component plus a single PL component, and its spectrum evolved significantly in the soft-X-rays as well as in the hard-X-ray data (Kuiper et al. 2012). Here, we only use the *XMM-Newton* observation executed on 2009 February 3, which is one week after the Suzaku observation (on 2009 January 28), and Γ of 1.41 is adopted based on the 15–70 keV Suzaku HXD-PIN data (Enoto et al. 2010b). The low energy portion of its spectrum is contaminated because the source is located at the center of SNR G327.24-013 (Gelfand & Gaensler 2007). Therefore, we again fit the 1.2–7.0 keV spectrum in order to eliminate large deviations owing to the contamination of diffuse nonthermal X-rays at the low energy (Figure 11). We find the best-fit parameters $nH = 4.77^{+0.13}_{-0.12} \times 10^{22}$ cm $^{-2}$, $kT = 0.50^{+0.03}_{-0.05}$ keV, $B = 8.98^{+0.36}_{-0.90} \times 10^{14}$ G, $\Delta\phi = 1.90^{+0.09}_{-0.73}$, $\beta = 0.19^{+0.03}_{-0.02}$, absorbed flux in 0.5–7.0 keV $F = 5.14 \times 10^{-11}$ erg cm $^{-2}$ s $^{-1}$, and $\chi^2/\text{dof} = 96.8/102$. Our modeling reveals that the STEMS3D component dominates the PL component below 7 keV (the flux ratio $\sim 3:1$).

The transient SGR SGR 0418+5729 was discovered on 2009 June 5 when its bursts triggered the Fermi/GBM, and then was reported as the first magnetar with a low inferred dipole magnetic field Rea et al. (2010). Based on its spectra, Güver et al. (2011) argued that the value

of the magnetic field at the surface is 10^{14} G based on the STEMS fitting. The strong magnetic field case in this source was later confirmed by Tiengo et al. (2013). Nevertheless, the STEMS3D model cannot provide an acceptable fit to the spectrum of SGR 0418+5729 (ObsID = 0610000601). The canonical (BB+PL) model results indicate that the overall flux is dominated by a very hot thermal component ($kT \sim 0.9$ keV). The STEMS fitting results show that the particle velocity is $\beta \sim 0.5$ and the optical depth in the magnetosphere is $\tau \sim 9$. However, as can be seen in the Figure 3, the optical depth in the STEMS3D model is governed by both β and $\Delta\phi$, and cannot be larger than two when the β is greater than 0.3.

The AXP CXOU J164710.2-455216 is located in the young massive stars cluster, Westerlund 1 (Muno et al. 2006). The source underwent the first intense outburst on 2006 September and the second one on 2011 September (Rodríguez Castillo et al. 2014). Measuring the spin period and period derivative, An et al. (2013) suggested that the spin-down inferred magnetic field strength is less than 7×10^{13} G. We attempted to fit six bright *XMM-Newton* pointing data during 2006 and 2011, and obtained statistically acceptable fits with $\chi^2/\text{dof} \sim 0.99$. However, the values of B in both STEMS and STEMS3D modeling peg at the low limit of 10^{14} G; therefore, the obtained parameters are not reliable. We, therefore, do not include this source for further discussion.

5. DISCUSSION

Table 5
Spectral parameters of 1E 2259+586.

Group	Obs No.	nH (10^{22} cm^{-2})	kT (keV)	B (10^{14} G)	$\Delta\phi$ (rad)	β	Flux	χ^2/dof
Group1	Obs1	$0.82^{+0.01}_{-0.01}$	$0.39^{+0.03}_{-0.05}$	$5.69^{+0.88}_{-0.43}$	$1.34^{+0.59}_{-0.59}$	$0.18^{+0.02}_{-0.02}$	2.52	871.1/928
...	Obs2	...	$0.35^{+0.01}_{-0.01}$	$6.01^{+0.26}_{-0.21}$	$1.45^{+0.04}_{-0.05}$	$0.20^{+0.01}_{-0.01}$	2.60	...
...	Obs3	...	$0.33^{+0.01}_{-0.01}$	$9.61^{+0.30}_{-0.28}$	$1.97^{+0.22}_{-0.22}$	$0.22^{+0.01}_{-0.01}$	5.62	...
...	Obs4	...	$0.36^{+0.08}_{-0.05}$	$6.14^{+0.94}_{-1.50}$	$1.10^{+0.46}_{-0.26}$	$0.23^{+0.01}_{-0.01}$	4.46	...
...	Obs5	...	$0.42^{+0.02}_{-0.03}$	$5.79^{+0.37}_{-0.41}$	$2.0^{+0.07}_{-0.4}$	$0.19^{+0.02}_{-0.02}$	4.59	...
...	Obs6	...	$0.38^{+0.02}_{-0.01}$	$5.03^{+0.25}_{-0.11}$	$1.90^{+0.07}_{-0.06}$	$0.20^{+0.01}_{-0.01}$	3.03	...
...	Obs7	...	$0.33^{+0.03}_{-0.02}$	$7.82^{+1.01}_{-0.75}$	$1.19^{+0.12}_{-0.30}$	$0.20^{+0.01}_{-0.01}$	2.96	...
...	Obs8	...	$0.37^{+0.02}_{-0.02}$	$5.01^{+0.81}_{-0.13}$	$1.91^{+0.11}_{-0.11}$	$0.20^{+0.01}_{-0.01}$	2.96	...
...	Obs9	...	$0.37^{+0.02}_{-0.04}$	$5.38^{+0.21}_{-0.53}$	$1.60^{+0.06}_{-0.23}$	$0.20^{+0.01}_{-0.01}$	2.94	...
...	Obs10	...	$0.36^{+0.04}_{-0.02}$	$5.87^{+0.51}_{-0.68}$	$1.46^{+0.23}_{-0.24}$	$0.21^{+0.01}_{-0.01}$	2.87	...
Group2	Obs1	$0.79^{+0.01}_{-0.01}$	$0.41^{+0.02}_{-0.05}$	$6.17^{+0.16}_{-0.13}$	$1.07^{+0.48}_{-0.36}$	$0.18^{+0.03}_{-0.02}$	2.52	930.0/937
...	Obs2	...	$0.37^{+0.01}_{-0.01}$...	$1.25^{+0.04}_{-0.11}$	$0.20^{+0.01}_{-0.01}$	2.60	...
...	Obs3	...	$0.40^{+0.01}_{-0.01}$...	$2.0^{+0.01}_{-0.1}$	$0.23^{+0.01}_{-0.01}$	5.63	...
...	Obs4	...	$0.38^{+0.02}_{-0.05}$...	$1.10^{+0.30}_{-0.12}$	$0.23^{+0.01}_{-0.01}$	4.46	...
...	Obs5	...	$0.43^{+0.02}_{-0.02}$...	$2.0^{+0.09}_{-0.3}$	$0.18^{+0.02}_{-0.02}$	4.59	...
...	Obs6	...	$0.37^{+0.01}_{-0.02}$...	$1.30^{+0.09}_{-0.09}$	$0.20^{+0.01}_{-0.01}$	3.03	...
...	Obs7	...	$0.36^{+0.02}_{-0.01}$...	$1.45^{+0.13}_{-0.26}$	$0.20^{+0.01}_{-0.01}$	2.96	...
...	Obs8	...	$0.35^{+0.02}_{-0.01}$...	$1.50^{+0.13}_{-0.26}$	$0.20^{+0.01}_{-0.01}$	2.96	...
...	Obs9	...	$0.37^{+0.01}_{-0.02}$...	$1.24^{+0.32}_{-0.08}$	$0.20^{+0.01}_{-0.01}$	2.94	...
...	Obs10	...	$0.37^{+0.01}_{-0.02}$...	$1.25^{+0.25}_{-0.27}$	$0.20^{+0.01}_{-0.01}$	2.87	...
Group3	Obs1/Obs2	$0.77^{+0.01}_{-0.01}$	$0.40^{+0.01}_{-0.01}$	$5.89^{+0.08}_{-0.08}$	$1.46^{+0.03}_{-0.03}$	$0.19^{+0.01}_{-0.01}$	2.56/2.60	976.4/949
...	Obs3	...	$0.43^{+0.01}_{-0.01}$...	$2.0^{+0.01}_{-0.1}$	$0.21^{+0.01}_{-0.01}$	5.63	...
...	Obs4/Obs5	...	$0.44^{+0.02}_{-0.01}$...	$1.96^{+0.07}_{-0.13}$	$0.18^{+0.01}_{-0.01}$	4.49/4.57	...
...	Obs6	...	$0.41^{+0.01}_{-0.01}$...	$1.85^{+0.07}_{-0.08}$	$0.17^{+0.01}_{-0.01}$	3.03	...
...	Obs7/Obs8	...	$0.39^{+0.02}_{-0.02}$...	$1.48^{+0.04}_{-0.04}$	$0.19^{+0.01}_{-0.01}$	2.96/2.97	...
...	Obs9/Obs10	...	$0.41^{+0.01}_{-0.02}$...	$1.23^{+0.04}_{-0.07}$	$0.20^{+0.01}_{-0.01}$	2.94/2.87	...

Note. — Flux: 0.5–7.0 keV absorbed flux in units of $10^{-11} \text{ erg cm}^{-2} \text{ s}^{-1}$. All errors are in the 90% confidence level. Group1: the only parameter of nH is linked for different observations in the simultaneous fit. Group2: both parameters of nH, and B are linked. Group3: three pairs of successive observations (Obs1/Obs2, Obs7/Obs8, and Obs9/Obs10) are merged.

Table 6
Spectral fit results of XTE J1810-197

Group	Obs No.	nH (10^{22} cm^{-2})	kT (keV)	B (10^{14} G)	$\Delta\phi$ (rad)	β	Flux	χ^2/dof
Group1	Obs1	$0.88^{+0.02}_{-0.02}$	$0.52^{+0.01}_{-0.01}$	$2.22^{+0.04}_{-0.04}$	$1.66^{+0.02}_{-0.02}$	$0.10^{+0.01}_{-0.01}$	3.76	559.7/442
...	Obs2	...	$0.50^{+0.01}_{-0.02}$	$2.44^{+0.06}_{-0.08}$	$1.98^{+0.06}_{-0.05}$	$0.10^{+0.01}_{-0.01}$	2.19	...
...	Obs3	...	$0.44^{+0.01}_{-0.01}$	$2.50^{+0.06}_{-0.06}$	$1.66^{+0.09}_{-0.04}$	$0.11^{+0.01}_{-0.01}$	1.32	...
...	Obs4	...	$0.34^{+0.01}_{-0.01}$	$2.61^{+0.04}_{-0.03}$	$1.64^{+0.03}_{-0.03}$	$0.10^{+0.01}_{-0.01}$	0.55	...
Group2	Obs1	$0.93^{+0.02}_{-0.01}$	$0.51^{+0.02}_{-0.01}$	$2.52^{+0.02}_{-0.02}$	$1.66^{+0.03}_{-0.02}$	$0.10^{+0.01}_{-0.01}$	3.74	750.7/448
...	Obs2	...	$0.49^{+0.01}_{-0.01}$	$0.10^{+0.01}_{-0.01}$	2.19	...
...	Obs3	...	$0.42^{+0.01}_{-0.01}$	$0.12^{+0.01}_{-0.01}$	1.32	...
...	Obs4	...	$0.32^{+0.01}_{-0.01}$	$0.10^{+0.01}_{-0.01}$	0.55	...

Note. — Flux: 0.5–7.0 keV absorbed flux in units of $10^{-11} \text{ erg cm}^{-2} \text{ s}^{-1}$. All errors are in the 90% confidence level. Group1: the only parameter of nH is linked for different observations in the simultaneous fit. Group2: parameters of nH, B , and $\Delta\phi$ are linked.

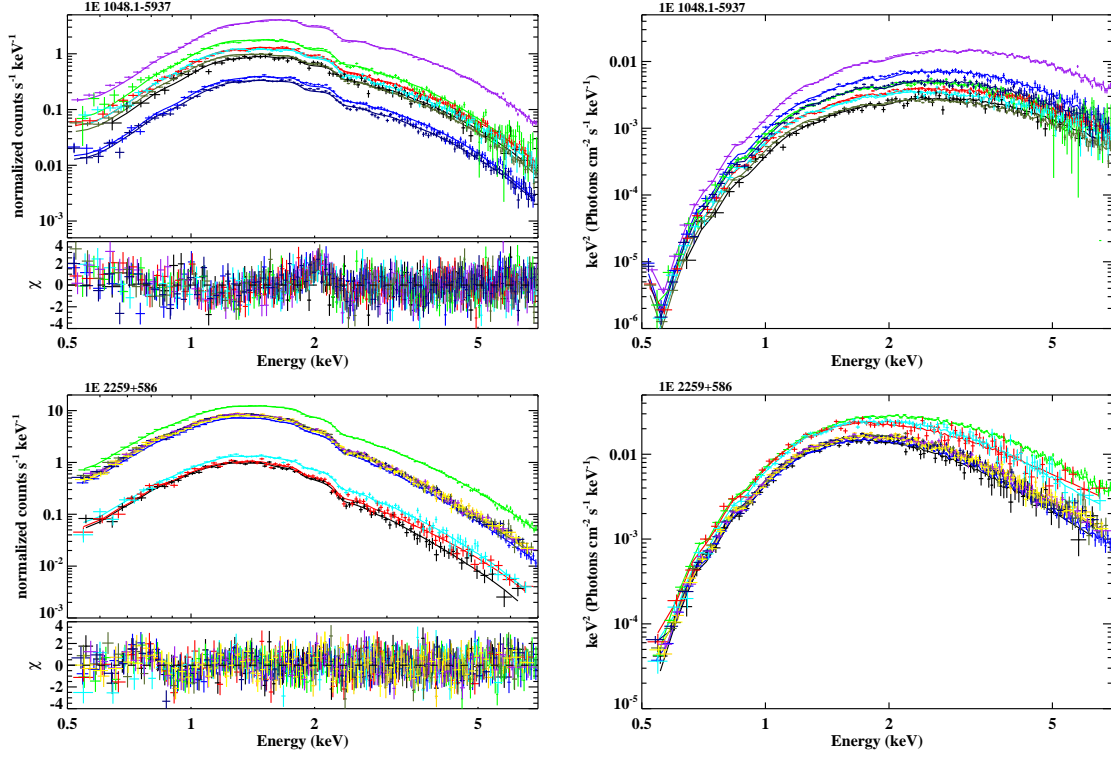


Figure 9. Same as Figure 6 but for 1E 1048.1-5937 and 1E 2259+586.

Table 7
Spectral fit results of SGR 0501+456

Group	Obs No.	nH (10^{22} cm^{-2})	kT (keV)	B (10^{14} G)	$\Delta\phi$ (rad)	β	Flux	χ^2/dof
Group1	Obs1	$0.96^{+0.01}_{-0.01}$	$0.44^{+0.01}_{-0.01}$	$2.28^{+0.07}_{-0.07}$	$1.51^{+0.06}_{-0.08}$	$0.206^{+0.005}_{-0.005}$	3.72	600.2/604
...	Obs2	...	$0.49^{+0.01}_{-0.01}$	$2.33^{+0.07}_{-0.07}$	$1.53^{+0.04}_{-0.08}$	$0.159^{+0.008}_{-0.008}$	3.13	...
...	Obs3	...	$0.50^{+0.02}_{-0.02}$	$2.34^{+0.06}_{-0.10}$	$1.71^{+0.05}_{-0.06}$	$0.150^{+0.013}_{-0.021}$	2.94	...
...	Obs4	...	$0.50^{+0.01}_{-0.02}$	$2.41^{+0.05}_{-0.08}$	$1.66^{+0.04}_{-0.14}$	$0.143^{+0.010}_{-0.016}$	2.65	...
...	Obs5	...	$0.44^{+0.01}_{-0.02}$	$2.41^{+0.08}_{-0.09}$	$1.65^{+0.08}_{-0.30}$	$0.144^{+0.013}_{-0.011}$	1.44	...
Group2	Obs1	$0.96^{+0.01}_{-0.01}$	$0.45^{+0.01}_{-0.01}$	$2.35^{+0.01}_{-0.04}$	$1.50^{+0.06}_{-0.06}$	$0.203^{+0.004}_{-0.010}$	3.72	605.9/608
...	Obs2	...	$0.49^{+0.01}_{-0.01}$...	$1.52^{+0.05}_{-0.08}$	$0.158^{+0.006}_{-0.006}$	3.13	...
...	Obs3	...	$0.50^{+0.01}_{-0.01}$...	$1.71^{+0.05}_{-0.06}$	$0.150^{+0.011}_{-0.019}$	2.94	...
...	Obs4	...	$0.49^{+0.01}_{-0.01}$...	$1.65^{+0.04}_{-0.13}$	$0.149^{+0.006}_{-0.006}$	2.65	...
...	Obs5	...	$0.43^{+0.01}_{-0.01}$...	$1.65^{+0.10}_{-0.33}$	$0.148^{+0.012}_{-0.010}$	1.44	...

Note. — Flux: 0.5–7.0 keV absorbed flux in units of $10^{-11} \text{ erg cm}^{-2} \text{ s}^{-1}$. All errors are in the 90% confidence level. Group1: the only parameter of nH is linked for different observations in the simultaneous fit. Group2: both parameters of nH, and B are linked.

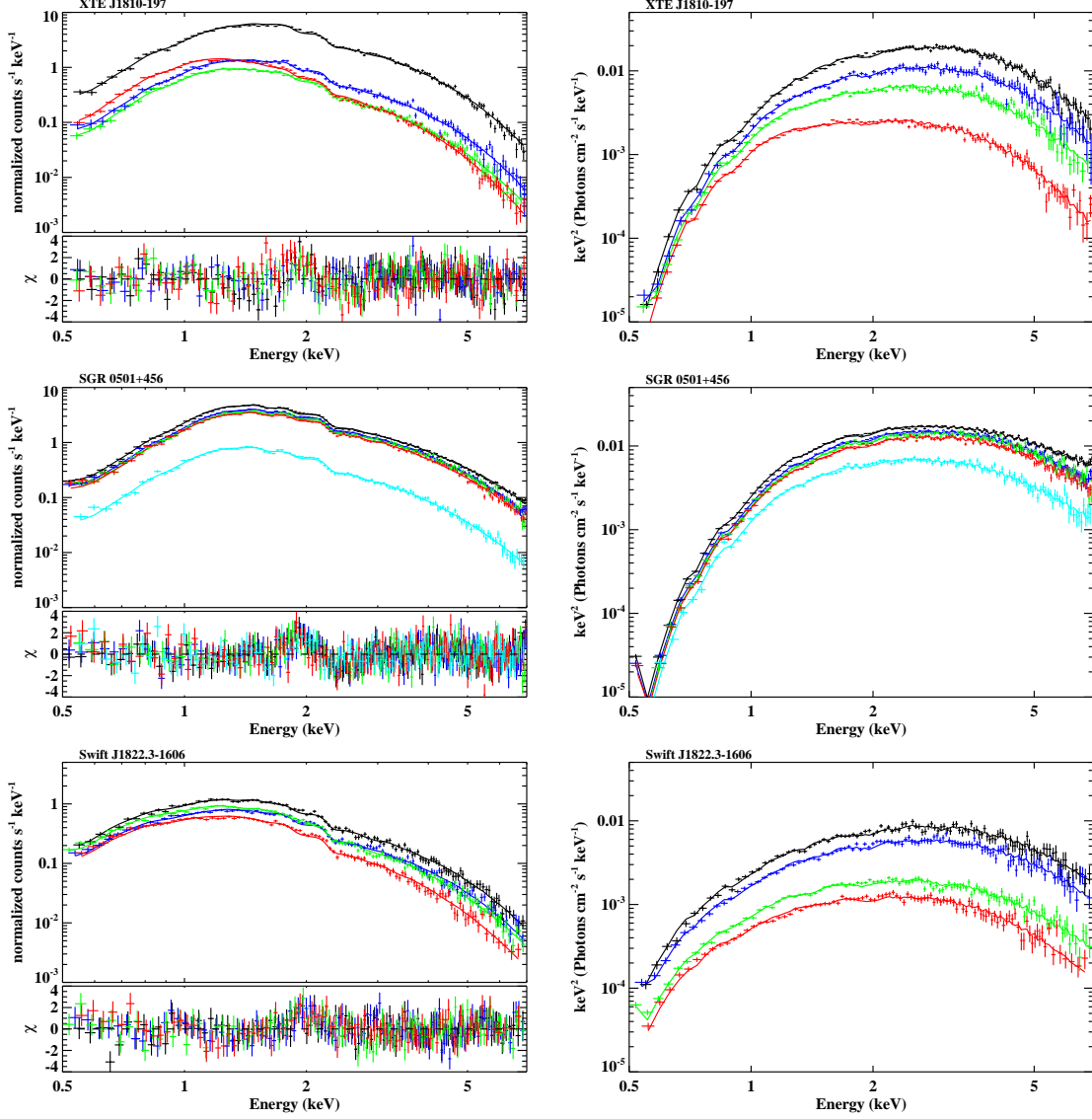


Figure 10. Same as Figure 6 but for transients XTE J1810-197, SGR 0501+456, and *Swift* J1822.3-1606.

Table 8
Spectral fit results of *Swift* J1822.3-1606

Group	Obs No.	nH (10^{22} cm^{-2})	kT (keV)	B (10^{14} G)	$\Delta\phi$ (rad)	β	Flux	χ^2/dof
Group1	Obs1	$0.42^{+0.01}_{-0.01}$	$0.54^{+0.02}_{-0.02}$	$2.31^{+0.07}_{-0.08}$	$1.42^{+0.04}_{-0.07}$	$0.12^{+0.03}_{-0.03}$	1.90	415.5/420
...	Obs2	...	$0.54^{+0.01}_{-0.02}$	$2.33^{+0.06}_{-0.04}$	$1.52^{+0.04}_{-0.06}$	$0.11^{+0.03}_{-0.03}$	1.31	...
...	Obs3	...	$0.45^{+0.02}_{-0.02}$	$2.34^{+0.08}_{-0.08}$	$1.80^{+0.04}_{-0.03}$	$0.13^{+0.01}_{-0.01}$	0.43	...
...	Obs4	...	$0.44^{+0.02}_{-0.02}$	$2.35^{+0.08}_{-0.09}$	$1.69^{+0.05}_{-0.04}$	$0.12^{+0.01}_{-0.01}$	0.28	...
Group2	Obs1	$0.42^{+0.01}_{-0.01}$	$0.54^{+0.01}_{-0.01}$	$2.32^{+0.04}_{-0.04}$	$1.42^{+0.04}_{-0.07}$	$0.12^{+0.01}_{-0.01}$	1.91	420.5/426
...	Obs2	...	$0.53^{+0.01}_{-0.01}$...	$1.51^{+0.04}_{-0.06}$...	1.31	...
...	Obs3	...	$0.46^{+0.01}_{-0.01}$...	$1.80^{+0.04}_{-0.03}$...	0.44	...
...	Obs4	...	$0.43^{+0.01}_{-0.01}$...	$1.69^{+0.05}_{-0.04}$...	0.28	...

Note. — Flux: 0.5–7.0 keV absorbed flux in units of $10^{-11} \text{ erg cm}^{-2} \text{ s}^{-1}$. All errors are in the 90% confidence level. Group1: the only parameter of nH is linked for different observations in the simultaneous fit. Group2: parameters of nH , B , and β are linked.

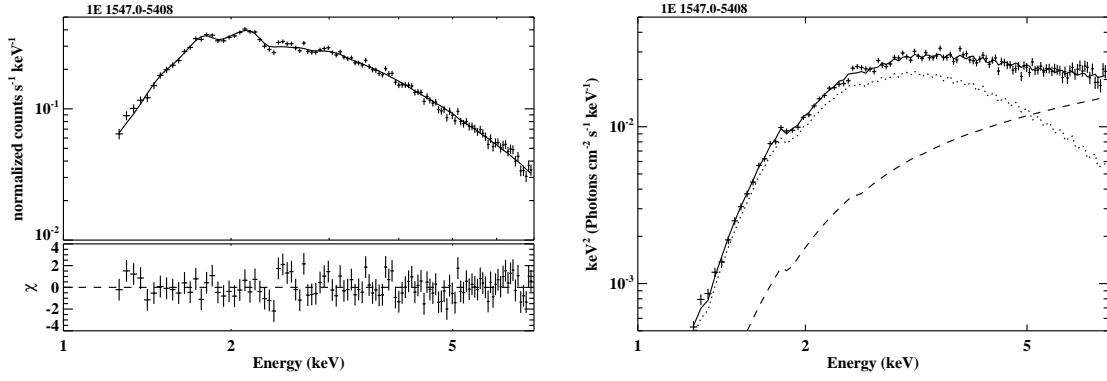


Figure 11. Same as Figure 6 but for the observation of 1E 1547.0-5408 taken on 2009 February 3.

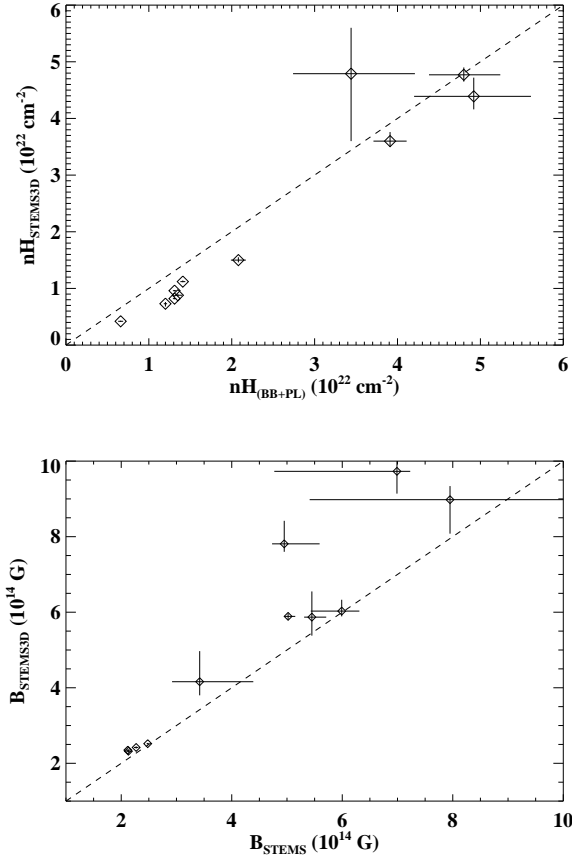


Figure 12. Upper panel: nH_{STEMS3D} vs. $nH_{\text{BB+PL}}$. Bottom panel: B_{STEMS3D} vs. B_{STEMS} .

Table 9
Log of the Magnetic Field

Source	B_{timing} (10^{14} G)	B_{STEMS} (10^{14} G)	B_{STEMS3D} (10^{14} G)
4U 0142+61	1.3 ^a	5.45 ^{+0.26} _{-0.14}	5.87 ^{+0.68} _{-0.49}
1RXS J170849.0-400910	4.6 ^b	5.99 ^{+0.32} _{-0.56}	6.03 ^{+0.30} _{-0.14}
1E 1841-045	6.9 ^b	3.42 ^{+0.97} _{-0.50}	4.16 ^{+0.81} _{-0.36}
CXOU J171405.7-381031	5.0 ^c	6.99 ^{+2.22} _{-0.64}	9.73 ^{+0.59} _{-0.21}
SGR 1900+14	7.0 ^d	4.95 ^{+0.22} _{-0.04}	7.81 ^{+0.61} _{-0.21}
1E 1048.1-5937	3.9 ^e	2.27 ^{+0.04} _{-0.04}	2.42 ^{+0.03} _{-0.03}
1E 2259+586	0.59 ^f	5.02 ^{+0.13} _{-0.07}	5.89 ^{+0.08} _{-0.08}
XTE J1810-197	2.1 ^g	2.48 ^{+0.02} _{-0.02}	2.52 ^{+0.02} _{-0.02}
SGR 0501+456	1.9 ^h	2.12 ^{+0.04} _{-0.04}	2.35 ^{+0.04} _{-0.04}
<i>Swift</i> J1822.3-1606	0.135 ⁱ	2.13 ^{+0.06} _{-0.04}	2.32 ^{+0.04} _{-0.04}
1E 1547.0-5408	3.2 ^j	7.95 ^{+0.36} _{-2.54}	8.98 ^{+0.36} _{-0.90}

Note. — Period derivatives of magnetars are highly variable, and the derived B_{timing} could be significantly different from the values listed here.

(a) Dib et al. 2007; (b) Dib et al. 2008; (c) Sato et al. 2010; (d) Mereghetti et al. 2006; (e) Dib et al. 2009; (f) Gavril & Kaspi 2002; (g) Camilo et al. 2007; (h) Göğüş et al. 2010; (i) Scholz et al. 2014; (j) Dib et al. 2012.

In this paper, we developed a physically motivated numerical model to account for the magnetar surface emission and magnetospheric scattering in three dimensions. We applied our model to the X-ray spectra of 13 magnetars, including persistent X-ray emitters as well as transient sources. We find that most spectra analyzed here were adequately described with the STEMS3D model, yielding important physical parameters, such as the surface magnetic field strengths and degree of twisting in the magnetosphere. To compare with our results, we also modeled all magnetar spectra with the STEMS model, which employs the same atmospheric emission properties, but incorporates an only 1D scattering scheme on the emergent radiation (Güver et al. 2007). We find that the surface magnetic field strengths obtained by fitting the STEMS3D model are generally slightly higher, but are still in agreement within errors with those obtained with the STEMS model (see the lower panel of Figure 12).

Dipole magnetic fields inferred from spin parameters (B_{timing}) in 7 out of the 11 sources are consistent with the values obtained from the STEMS3D model fitting (Table 9). The STEMS3D model does not provide an acceptable fit to the spectrum of the first low- B magnetar, SGR 0418+5729, for reasons as already discussed in §4.2.3. While for another two magnetars with $B_{\text{timing}} < 10^{14}$ G, 1E 2259+586 and *Swift* J1822.3-1606, the strengths of B given by the STEMS3D model are about one order of magnitude higher than their dipole magnetic fields. However, taking both twisted magnetospheres (Thompson et al. 2002; Beloborodov 2009) and particle outflows (Tong et al. 2013) into account, the expected spin-down torque (\dot{P}) will be larger than a pure dipole case with the same poloidal magnetic field. The conflict between larger values of B_{STEMS3D} and timing results could be reconciled by either a small magnetic inclination angle (e.g., Tong & Xu 2012) and/or a more complex structure of magnetosphere (i.e., higher order multipoles). In a multipolar field, the strong surface magnetic field decays more rapidly with radius; thus, a too fast spin-down rate can be avoided (Turolla et al. 2011).

On the other hand, an important caveat for the inferred dipole field is that, magnetars are very noisy and their period derivatives can vary significantly within a short timescale (e.g., Archibald et al. 2015, and references therein), leading to fluctuations in B_{timing} , which is unphysical. For example, Livingstone et al. (2011) measured a spin-down rate of $\dot{P} = 2.54 \times 10^{-13} \text{ s s}^{-1}$ using data collected in the first four months following the 2011 July outburst of *Swift* J1822.3-1606. Rea et al. (2013) estimated $\dot{P} = 8.32 \times 10^{-14} \text{ s s}^{-1}$ with the data covering 2011 July – 2012 April, and recently Scholz et al. (2014) took the new *Swift* data into account and reported $\dot{P} = 2.15 \times 10^{-14} \text{ s s}^{-1}$. As a consequence, the corresponding B_{timing} decreased from the previous value of 4.7×10^{13} G to 1.4×10^{13} G listed in Table 9. The decreasing spin-down rate can be interpreted as either a sign of wind braking (Tong & Xu 2013) or a glitch recovery (Scholz et al. 2014). Our spectral investigations with the STEMS3D, however, yields magnetar-like surface magnetic field strength (2.3×10^{14} G), which is likely the case given that, at the very least, the source exhibited

energetic bursts.

We find that the temperatures of the magnetar surfaces vary between 0.24 and 0.56 keV, and the magnetospheric electrons are non-relativistic ($\beta \leq 0.2$). We investigated multiple *XMM-Newton* observations typically spanning years of five magnetars and find that the strength of the surface magnetic fields remains nearly constant. We also modeled all magnetar spectra with the phenomenological (BB+PL) model to better establish the interstellar absorption aspects toward magnetars studied here. It is well known that the simple PL model increases very rapidly at low energies, and as a consequence, a larger absorption column density is required to account for the overestimated PL flux, especially for the steep PL indices (Durant & van Kerkwijk 2006; Güver et al. 2008). In all sources except 1E 1841-045, the hydrogen column density obtained from the STEMS3D model fits (nH_{STEMS3D}) is lower than the value derived from the (BB+PL) model fits ($nH_{\text{(BB+PL)}}$; Figure 12). We argue that, given the empirical nature of the (BB+PL) model, the density of interstellar hydrogen obtained with the STEMS3D is a more reliable indicator.

As already stated, the surface magnetic field values from the STEMS3D model mostly agree with those obtained with the STEMS model results (Table 9). However, the STEMS model makes simplifying assumptions about the magnetic field geometry, i.e., treating the scattering region as a plane-parallel slab; therefore, it cannot offer information about the geometry of the magnetosphere. Alternatively, the 3D self-similar magnetic configuration is characterized by a free parameter, $\Delta\phi$, in the STEMS3D model. Our fitting results indicate that the magnetospheres in most magnetars are highly twisted ($\Delta\phi \geq 1$). It is worth noting that we also included a flat PL ($\Gamma = 1.32$) component in the fitting for 1E 1841-045, which could be the reason why it has a large value of nH_{STEMS3D} . The derived small magnetospheric twist angle $\Delta\phi = 0.31^{+0.80}_{-0.11}$ and large $\beta = 0.28^{+0.04}_{-0.06}$ should be treated with caution, and longer exposure observations are required to check the magnetospheric parameters of 1E 1841-045 in the future.

Compared with the STEMS model, the STEMS3D model embodies some other significant improvements: (1) in the 1D geometry, the magnetic field is fixed to follow a $\mathbf{B} \propto r^{-3}$ dependence, and the optical depth τ is independent of the electron velocity β . In contrast, the radial dependence of the magnetic field is consistently obtained from $\Delta\phi$, while the angle-averaged optical depth τ is determined by β and $\Delta\phi$. (2) The charged particles are assumed to have a top-hat velocity distribution in the 1D model, while a more realistic distribution, involving the effects of bulk motion and also thermal velocity distribution of electrons, is used in the STEMS3D model. Following the work in Nobili et al. (2008), we adopt the 1D Maxwellian distribution at the electron temperature T_e , which is further linked with β by assuming equipartition between thermal and bulk kinetic energy in order to reduce the number of parameters in the model. (3) In the 3D configuration, the optical depth varies significantly with angles and vanishes at magnetic poles in the twisted magnetosphere. Thus, it is possible to detect the surface radiation which is mostly carried by extraordinary mode photons, if one of the magnetic poles is in our

line of sight. The polarization and the proton cyclotron absorption lines are expected to vary with the rotational phase. Note that Tiengo et al. (2013) recently reported a phase-variable absorption feature observed during the outburst of SGR 0418+5729.

We also aimed to understand the nature of variable and transient magnetars by investigating their spectral evolution. For this purpose, we analyzed multiple *XMM-Newton* observations of six magnetars. 1E 1048.1-5937 has been quite active in the past 10 yr: three X-ray flares were recorded with RXTE in 2001, 2002, and 2007 March (Dib et al. 2009). The eight *XMM-Newton* observations we used here are sampled before, after and in between these flares: Obs1 was performed before the first flare; Obs2-5 were executed between the second and third flares; Obs6-7 were performed after the third flare; comparing with Obs7, the source brightened by a factor of two in Obs8 (on 2013 July 22, after the end of RXTE mission). We find that the surface temperature monotonically decreases with declining flux from Obs2 to Obs5 and from Obs6 to Obs7 (see Group 1-3 in Table 4). This is likely due to cooling of the NS crust that is heated by the mechanism leading to these flares. However, the magnetospheric twist angle cannot be constrained in this source.

In the magnetar framework, both the crustal cooling (e.g., Pons & Rea 2012) and the magnetospheric relaxation (e.g., Bernardini et al. 2009) models are proposed for the flux relaxation in different sources. The dense *XMM-Newton* observations on 1E 2259+586 provide a good opportunity to study this topic. The first two data sets are observed before the burst event, and the other eight observations monitored the flux relaxation of the outburst in the following three years. The STEMS3D fitting results suggest a large magnetic field $\sim 5.9 \times 10^{14}$ G for the source, and the $\Delta\phi$ suddenly increased to a maximum from Obs2 to Obs3 then decreased following the flux decays. The only exception, Obs4, which was executed ~ 20 days after the burst, has a small $\Delta\phi = 1.1$. Note that, Obs4 and Obs5 were performed on the same day; however, the latter yields a large $\Delta\phi \sim 2$. Such a small discrepancy between Obs4 and Obs5 was also seen in the (BB+PL) fitting results (Zhu et al. 2008), i.e., the flux ratio between PL and BB components varied from 2.6 (Obs4) to 2.1 (Obs5). It is not likely that the magnetosphere could untwist and retwist in a few days, and the small $\Delta\phi$ derived from Obs4 is dubious. Group 2 in Table 5 shows a strong correlation between $\Delta\phi$ and flux with the Spearman's rank correlation coefficient of $\rho/P = 0.661/0.038$. Since the Spearman's rank correlation coefficient does not consider the parameter uncertainties, it would underestimate the significance level due to the spectral fluctuations. Therefore, we merge three pairs of observations (Obs1/Obs2, Obs7/Obs8, and Obs9/Obs10) that have similar spectral parameters and flux levels, as well as Obs4/Obs5, and the correlation between $\Delta\phi$ and flux becomes more significant ($\rho/P = 0.942/0.005$, Group 3 in Table 5). When $\Delta\phi$ is linked, the χ^2 increases by more than 51.9, which suggests the significant variation of $\Delta\phi$ with an F-test probability lower than 2×10^{-9} . Therefore, our finding of an increased twist angle accompanied with the outburst (occurred between Obs2 and Obs3)

and then a decrease following the source decays, agrees perfectly with the twisted/untwisted magnetosphere scenario (Thompson et al. 2002).

The STEMS3D fitting results of both XTE J1810-197 and *Swift* J1822.3-1606 show that the surface temperature monotonically declines with decreasing luminosity. The former source had been studied in detail with the STEMS model (Güver et al. 2007). On the other hand, it is the first time that we evaluated the surface magnetic field of *Swift* J1822.3-1606 via continuum-fitting, and obtained a significantly stronger magnetic field than the dipole magnetic field inferred from the spin-down rate (Scholz et al. 2014). It is interesting to note that XTE J1810-197 and *Swift* J1822.3-1606 share the similar spectral sequences following their outbursts (Rea et al. 2012; Scholz et al. 2014). Nevertheless, the timing analyses infer a typical magnetar magnetic field for XTE J1810-197 ($B_{\text{timing}} \sim 2.1 \times 10^{14}$ G, Camilo et al. 2007) while a low value for the latter source ($B_{\text{timing}} \sim 1.4 \times 10^{13}$ G, Scholz et al. 2014). Our spectroscopic measurements suggest a similar magnetic field strength of $B_{\text{STEMS3D}} \sim 2.3 \times 10^{14}$ G for these two transients. The monotonic decline of surface temperatures during the outburst decays in both XTE J1810-197 and *Swift* J1822.3-1606 are remarkable evidence of crustal cooling (Güver et al. 2007; Scholz et al. 2014). Additionally, we also find a significant variation of $\Delta\phi$ in *Swift* J1822.3-1606 (with a confidence of 99.5%). We also find a decline of the magnetospheric electron velocity β in the first ~ 40 days of the 2008 outburst of SGR 0501+456 (Table 7), implying the energy dissipation of charged particles, probably by the radiative drag.

Different scenarios have been proposed to account for the hard-X-ray emissions from magnetars. Thompson & Beloborodov (2005) put forward two mechanisms that soft- γ -rays either arise from the thermal bremsstrahlung emissions in a thin surface layer heated by a returning current or the synchrotron emissions from e^\pm pairs (see also Beloborodov & Thompson 2007). Alternatively, Baring & Harding (2007) suggested that the high energy tail was produced by the resonant up-scattering in the magnetosphere. The 3D Monte Carlo simulations show that the soft-X-ray photons can be up-scattered to ~ 100 keV if the scattering particles are energetic, i.e., $\beta > 0.6$ and the corresponding electron temperature $kT_e > 100$ keV (Nobili et al. 2008; Zane et al. 2009). However, our spectral analysis shows that the $\Delta\phi > 1$ and the $\beta \sim 0.2$ in most cases, while flatter spectra and stronger pulsations detected at the hard-X-ray clearly point to a different population of electrons. Beloborodov (2013) proposed that e^\pm pairs discharge near the neutron star and create the relativistic outflow that further scatters thermal photons to high energies. This model provided a satisfactory explanation for the hard-X-ray luminosity, spectral slopes, and pulsed profiles (e.g., Hascöet et al. 2014; Vogel et al. 2014), and it may also contribute an non-negligible flux in the soft-X-ray band.

It should be noted that the STEMS3D model still has some limitations, as other magnetospheric scattering models do (see Zane et al. 2009 and Beloborodov 2013). Both spectral and temporal analyses have demonstrated that the thermal emission is not uniformly dis-

tributed on the surface of magnetars but are confined in a small region (e.g., Özel 2002; Albano et al. 2010). However, because the uniform distribution is adopted for the seed photons, the STEMS3D model cannot provide an acceptable fit to the spectra of magnetars in quiescence, which lacks nonthermal emission. As the transients return to the quiescent state, the spectra of the three transients studied in our paper (i.e., XTE J1810-197, SGR 0501+456, and *Swift* J1822.3-1606) became significantly softer than those at outburst levels, and the second or even third thermally emitting surface regions were reported (Bernardini et al. 2009; Camero et al. 2014; Scholz et al. 2014). According to the (BB+BB) or (BB+PL) fits, it is found that the thermal emitting area decreases following the outburst decay. In these cases, the distinctive spectra would be formed for the following reasons: (i) In the 3D twisted magnetosphere, the optical depth and upscattering efficiency vary with latitude because the current density and direction (along the magnetic field line) depend on the position. The optical depth has a maximum and a minimum at the equator and the poles (no current exists along the magnetic axis), respectively. Thus, a hot spot presented at the pole would gain less energy from particles in the magnetosphere, resulting in a soft spectrum. (ii) Photons would be scattered away from the initial propagation directions and might move into or out of the sight of view. The viewing effect should be taken into account. (iii) The superposition of two thermal components at different temperatures modifies the spectral profile further. To date, however, it is impossible to incorporate all of these effects since it will involve too many parameters. We emphasize that those extremely soft spectra at very low flux levels cannot be fitted by the STEMS3D model nor the other normal Compton scattering models (e.g., 1D RCS, 3D RCS, STEMS models). Nevertheless, Zane et al. (2009) claimed that a softer spectrum is caused by a non-homogeneous distribution of surface emission (effects (i) and (ii)). Meanwhile, Turolla et al. (2011) also suggested that a surface thermal component dominated spectrum can be reproduced by considering effects (i) and (iii).

Beloborodov (2009) argued that the puzzling behavior of XTE J1810-197 can be explained with a untwisting magnetosphere, which is divided into a current-free (“cavity”) region and a current-carrying bundle (“j-bundle”) of field lines. The hot spot in the polar region is interpreted as the footprint of the j-bundle, which shrinks with time. As the magnetosphere untwists, the cavity expands and the j-bundle becomes so narrow that only a small fraction of the surface radiation can be scattered, producing very soft spectra in quiescence. However, in this model it is difficult to explain that lack of flux enhancement when glitches occurred in the stable sources. Alternatively, Pons & Rea (2012) interpreted transient behaviors as the magneto-thermal evolution, and suggested that short X-ray bursts and glitches might always be accompanied by a flux variation; nevertheless, the long-term flux of bright/stable magnetars (e.g., 4U 0142+61) cannot be enhanced significantly.

In some cases, magnetic configurations might be more complex than a dipole, and multipoles fields are required to avoid too fast spin-down as we discussed above.

In addition, the theoretical calculation indicates that the output luminosity from a globally twisted magnetosphere with $\Delta\phi > 1$ would be at the order of 10^{36} erg s⁻¹, which is higher than the observed (Thompson et al. 2002; Beloborodov 2009). There are now some observational phenomena in favor of partially, instead of globally, twisted magnetospheres (e.g., Woods et al. 2007; Pavan et al. 2009), which have been considered in the literature (Beloborodov 2009). Finally, although we make an assumption of constant velocity for charged particles, the particles should be decelerated via scattering of photons, broadening their velocity distribution.

We thank the anonymous referee for helpful comments and suggestions. We also thank Feryal Özel for providing the highly magnetized NS surface emission code, insightful discussions, and comments. S.S.W. is supported by the Scientific and Technological Research Council of Turkey (TÜBİTAK) and EC-FP7 Marie Curie Actions- People-COFUND Brain Circulation Scheme (2236).

REFERENCES

- Aharonian, F., Akhperjanian, A. G., Barres de Almeida, U., et al. 2008, *A&A*, 486, 829
- Albano, A., Turolla, R., Israel, G. L., et al. 2010, *ApJ*, 722, 788
- An, H., Kaspi, V. M., Archibald, R., & Cumming, A. 2013, *ApJ*, 763, 82
- An, H., Kaspi, V. K., Beloborodov, A. M., et al. 2014, *ApJ*, 790, 60
- Archibald, R. F., Kaspi, V. K., Ng, C.-Y., et al. 2015, *ApJ*, 800, 33
- Arnaud, K. A. 1996, in *ASP Conf. Ser. 101, Astronomical Data Analysis Software and Systems V*, ed. G. Jacoby & J. Barnes (San Francisco: ASP), 17
- Baring M. G., & Harding A. K., 2007, *Ap&SS*, 308, 109
- Beloborodov, A. M. 2009, *ApJ*, 703, 1044
- Beloborodov, A. M. 2013, *ApJ*, 762, 13
- Beloborodov, A. M., & Thompson, C. 2007, *ApJ*, 657, 967
- Bernardini, F., Israel, G. L., Dall’Osso, S., et al. 2009, *A&A*, 498, 195
- Bernardini, F., Perna, R., Gotthelf, E. V., et al. 2011, *MNRAS*, 418, 638
- Camero, A., Papitto, A., Rea, N., et al. 2014, *MNRAS*, 438, 3291
- Camilo, F., Cognard, I., Ransom, S. M., et al. 2007, *ApJ*, 663, 497
- den Hartog, P. R., Kuiper, L., Hermsen, W., et al. 2008a, *A&A*, 489, 245
- den Hartog P. R., Kuiper L., Hermsen W., 2008b, *A&A*, 489, 263
- Dib, R., Kaspi, V. M., & Gavril, F. P. 2007, *ApJ*, 666, 1152
- Dib, R., Kaspi, V. M., & Gavril, F. P. 2008, *ApJ*, 673, 1044
- Dib, R., Kaspi, V. M., & Gavril, F. P. 2009, *ApJ*, 702, 614
- Dib, R., Kaspi, V. M., Scholz, P., & Gavril, F. P. 2012, *ApJ*, 748, 3
- Durant M., & van Kerkwijk M. H., 2006, *ApJ*, 650, 1082
- Enoto, T., Nakazawa, K., Makishima, K., et al. 2010a, *ApJL*, 722, L162
- Enoto, T., Nakazawa, K., Makishima, K., et al. 2010b, *PASJ*, 62, 475
- Fernández, R., & Thompson, C., 2007, *ApJ*, 660, 615
- Gavril, F. P., Dib, R., Kaspi, V. M., et al. 2011, *ApJ*, 736, 138
- Gavril, F. P., & Kaspi, V. M. 2002, *ApJ*, 567, 1067
- Gögüş, E., Woods, P. M., Kouveliotou, C., et al. 2010, *ApJ*, 722, 899
- Gonzalez, M. E., Dib, R., Kaspi, V. M., et al. 2010, *ApJ*, 716, 1345
- Gotthelf, E. V., & Halpern, J. P. 2005, *ApJ*, 632, 1075
- Gelfand, J. D., & Gaensler, B. M. 2007, *ApJ*, 667, 1111
- Güver, T., Gögüş, E., Özel, F., 2011, *MNRAS*, 418, 2773
- Güver, T., Gögüş, E., Özel, F., 2012, *MNRAS*, 424, 210
- Güver, T., Özel, F., & Gögüş, E. 2008, *ApJ*, 675, 1499
- Güver, T., Özel, F., Gögüş, E., & Kouveliotou, C. 2007, *ApJL*, 667, L73
- Halpern, J. P., & Gotthelf, E. V. 2005, *ApJ*, 618, 874
- Heyl J. S., & Hernquist L., 1998, *MNRAS*, 300, 599
- Ho, W. C. G., & Lai, D. 2003, *MNRAS*, 338, 233
- Hascoët, R., Beloborodov, A. M., & den Hartog, P. R. 2014, *ApJL*, 786, L1
- Ibrahim, A. I., Markwardt, C. B., Swank, J. H., et al. 2004, *ApJL*, 609, L21
- Israel, G. L., Esposito, P., Rea, N., et al. 2010, *MNRAS*, 408, 1387
- Israel, G. L., Romano, P., Mangano, V., et al. 2008, *ApJ*, 685, 1114
- Kaneko, Y., Gögüş, E., Kouveliotou, C., et al. 2010, *ApJ*, 710, 1335
- Kaspi, V. M., & Boydstun, K. 2010, *ApJL*, 710, L115
- Kaspi, V. M., Gavril, F. P., Woods, P. M., et al. 2003, *ApJL*, 588, L93
- Kaspi, V. M., Lackey, J. R., & Chakrabarty, D. 2000, *ApJL*, 537, L31
- Kuiper, L., Hermsen, W., den Hartog, P. R., & Collmar, W. 2006, *ApJ*, 645, 556
- Kuiper, L., Hermsen, W., den Hartog, P. R., & Urama, J. O., 2012, *ApJ*, 748, 133
- Kuiper, L., Hermsen, W., & Méndez, M. 2004, *ApJ*, 613, 1173
- Kumar, H. S., Ibrahim, A. I., & Safi-Harb, S. 2010, *ApJ*, 716, 97
- Lamb, R. C., & Markert, T. H. 1981, *ApJ*, 244, 94
- Lin, L., Gögüş, E., Güver, T., & Kouveliotou, C. 2012, *ApJ*, 761, 132
- Livingstone, M. A., Scholz, P., Kaspi, V. M., Ng, C.-Y., & Gavril, F. P. 2011, *ApJL*, 743, L38
- Lodders, K. 2003, *ApJ*, 591, 1220
- Lyubarsky, Y., Eichler, D., & Thompson, C. 2002, *ApJL*, 580, L69
- Lyutikov, M., & Gavril, F. P. 2006, *MNRAS*, 368, 690
- Marsden, D., & White, N. E. 2001, *ApJL*, 551, L155
- Mereghetti, S. 2008, *A&ARv*, 15, 225
- Mereghetti, S., Esposito, P., Tiengo, A., et al., 2006, *ApJ*, 653, 1423
- Mereghetti, S., Götz, D., Weidenspointner, G., et al. 2009, *ApJL*, 696, L74
- Mereghetti, S., Tiengo, A., Esposito, P., et al., 2005, *ApJ*, 628, 938
- Muno, M. P., Gaensler, B. M., Clark, J. S., et al. 2007, *MNRAS*, 378, L44
- Muno, M. P., Clark, J. S., Crowther, P. A., et al. 2006, *ApJL*, 636, L41
- Ng, C.-Y., Kaspi, V. M., Dib, R., et al. 2011, *ApJ*, 729, 131
- Nobili, L., Turolla, R., & Zane, S. 2008, *MNRAS*, 386, 1527
- Olausen, S. A., & Kaspi, V. M. 2014, *ApJS*, 212, 6
- Özel, F. 2001, *ApJ*, 563, 276
- Özel, F. 2002, *ApJ*, 575, 397
- Özel, F. 2003, *ApJ*, 583, 402
- Pavan L., Turolla R., Zane S., Nobili L., 2009, *MNRAS*, 395, 753
- Pons, J. A., & Rea, N. 2012, *ApJL*, 750, L6
- Rea, N. 2014, *AN*, 335, 329
- Rea, N., & Esposito, P. 2011, in *High-Energy Emission from Pulsars and Their Systems*, ed. D. F. Torres & N. Rea (Berlin: Springer), 247
- Rea, N., Esposito, P., Turolla, R., et al. 2010, *Sci*, 330, 944
- Rea, N., Israel, G. L., Esposito, P., et al. 2012, *ApJ*, 754, 27
- Rea, N., Israel, G., Pons, J. A., et al. 2013, *ApJ*, 770, 65
- Rea, N., Zane, S., Turolla, R., Lyutikov, M., Götz, D., 2008, *ApJ*, 686, 1245
- Rodríguez Castillo, G. A., Israel, G. L., Esposito, P., et al. 2014, *MNRAS*, 441, 1305
- Sato T., Bamba A., Nakamura R., et al. 2010, *PASJ*, 62, L33
- Şaşmaz Muş S., Aydın B., & Gögüş E., 2014, *MNRAS*, 440, 2916
- Şaşmaz Muş S., & Gögüş E., 2013, *ApJ*, 778, 156
- Scholz, P., Kaspi, V. M., & Cumming, A. 2014, *ApJ*, 786, 62
- Strohmayer, T. E., & Ibrahim, A. I. 2000, *ApJL*, 537, L111
- Thompson, C., & Beloborodov, A. M. 2005, *ApJ*, 634, 565
- Thompson, C., & Duncan, R. C. 1995, *MNRAS*, 275, 255
- Thompson, C., & Duncan, R. C. 1996, *ApJ*, 473, 322
- Thompson, C., Lyutikov, M., Kulkarni, S.R., 2002, *ApJ*, 574, 332
- Tiengo, A., Esposito, P., Mereghetti, S., et al. 2013, *Natur*, 500, 312
- Tong, H., & Xu, R. X. 2012, *ApJL*, 757, L10
- Tong, H., & Xu, R. X. 2013, *RAA*, 13, 1207

- Tong, H., Xu, R. X., Peng, Q. H., & Song, L. M. 2010, RAA, 10, 553
- Tong, H., Xu, R. X., Song, L. M., & Qiao, G. J. 2013, ApJ, 768, 144
- Turolla, R., Zane, S., Pons, J. A., et al. 2011, ApJ, 740, 105
- Vasisht, G., & Gotthelf, E. V. 1997, ApJL, 486, L129
- Viganò, D., Rea, N., Pons, J. A., et al. 2013, MNRAS, 434, 123
- Vogel, J. K., Hascoët, R., Kaspi, V. M., et al. 2014, ApJ, 789, 75
- Vrba, F. J., Henden, A. A., Luginbuhl, C. B., Guetter, H. H., Hartmann, D. H., & Klose, S. 2000, ApJL, 533, L17
- Wang, W., Tong, H., & Guo, Y.J. 2014, RAA, 14, 673
- Wang, Z., & Chakrabarty, D. 2002, ApJL, 579, L33
- Woods, P. M., Kaspi, V. M., Thompson, C., et al. 2004, ApJ, 605, 378
- Woods P. M., Kouveliotou C., Finger M. H., et al. 2007, ApJ, 654, 470
- Woods, P. M., Kouveliotou, C., Gavril, F. P., et al. 2005, ApJ, 629, 985
- Woods, P., & Thompson, C. 2006, in Compact Stellar X-Ray Sources, ed. W. H. G. Lewin & M. van der Klis (Cambridge: Cambridge Univ. Press), 547
- Zane, S., Rea, N., Turolla, R., & Nobili, L. 2009, MNRAS, 398, 1403
- Zane, S., Turolla, R., Stella, L., & Treves, A. 2001, ApJ, 560, 384
- Zhou, P., Chen, Y., Li, X.-D., et al. 2014, ApJL, 781, L16
- Zhu, W., Kaspi, V. M., Dib, R., et al. 2008, ApJ, 686, 520